Advances in Applied Mathematics and Mechanics
Adv. Appl. Math. Mech., Vol. **xx**, No. x, pp. 1-31

DOI: 10.4208/aamm.OA-2022-0299
xxx 202x

A Study of Fifth-Order WENO Reconstruction for Genuinely Two-Dimensional Convection-Pressure Flux Split Riemann Solver

Shide Tan[1], Haizhuan Yuan[1,*] and Lijun Hu[2,3]

[1] *School of Mathematics and Computational Science, Xiangtan University, Xiangtan, Hunan 411105, China*
[2] *College of Mathematics and Statistics, Hengyang Normal University, Hengyang, Hunan 421002, China*
[3] *Hunan Key Laboratory for Computation and Simulation in Science and Engineering, Xiangtan University, Xiangtan, Hunan 411105, China*

Received 16 November 2022; Accepted (in revised version) 26 April 2023

Abstract. Although the genuinely two-dimensional HLL-CPS solver holds the inherent multidimensionality property and capability of resolving contact discontinuities, the conventional low-order (second-order and below) reconstruction methods still limits its application in the two-dimensional complex flows involving shock waves and shear layers. A fifth-order reconstruction method is proposed for the genuinely two-dimensional HLL-CPS solver. The conserved variable vectors at the midpoints of interfaces are approximated by the fifth-order 1D WENO reconstruction. Meanwhile, variables at the corners are evaluated by a dimension-by-dimension reconstruction method consisting of a number of 1D fifth-order WENO sweeps. To avoid introducing spurious oscillations, each reconstruction is carried out in the corresponding local characteristic fields. Numerical results of several benchmark tests indicate the higher-order accuracy and the multidimensionality property of the proposed scheme. Compared with the 1D HLLE, HLLC and HLL-CPS schemes, the proposed high-order genuinely two-dimensional HLL-CPS solver provides higher resolution for contact discontinuities and presents better robustness against the shock anomalies.

AMS subject classifications: 65M10, 78A48

Key words: Genuinely two-dimensional HLL-CPS solver, WENO, fifth-order, dimension-by-dimension reconstruction.

*Corresponding author.
Emails: tanshide89@163.com (S. Tan), yhz@xtu.edu.cn (H. Yuan), hulijun@lsec.cc.ac.cn (L. Hu)

1 Introduction

Due to ease of implementation and satisfying physical properties, the Godunov-type numerical methods [26] based on approximated Riemann solver have become very popular in the simulations of compressible flows. The representatives of Godunov-type numerical schemes include the Roe's scheme [44], the AUSM-type schemes [35,41], the flux vector splitting (FVS) schemes [54,57], the HLL scheme [29], the HLLC scheme [56] and the Osher scheme [23]. Among them, the HLL Riemann solver has been widely used to solve different hyperbolic systems because of its simplicity and satisfying the entropy condition. However, the conventional HLL solver is incapable of resolving contact waves. In order to remove the limitation of the HLL solver, Mandal and Panwar [39] proposed the HLL-CPS scheme, in which flux vectors are split into convective and pressure components and the density difference of the dissipation term in the pressure flux term is replaced by the pressure difference to improve the resolution for contact waves. Furthermore, it has been proved to have the additional advantage of suppressing numerical shock instability [40].

Although the applicability of Riemann solvers mentioned above has been verified by a large number of numerical testes, some researchers indicated that the 1D Riemann solvers lose their efficiency in multidimensional problems since they can not pick up the flow information traveling along the transverse direction of a local interface. Therefore, many practitioners have attempted to construct genuinely two-dimensional Riemann solvers. Some of early works included the corner transport method by Collela [20], the introduction of multidimensionality into 1D solvers [45], the weighted average flux method proposed by Billet and Toro [16], Leveque's multidimensional wave propagation algorithm [36], Wendroff's HLLE solver for multidimensional hypersonic conservative laws [59], the multidimensional linearized Roe scheme by Fey [24] and Brio [19]. Compared with the traditional 1D solvers, the multidimensional solvers show some advantages in terms of accuracy. However, the mathematical complexity and high computational cost have limited their application in the simulations of complex flow problems.

Based on the idea of solving the two-dimensional Riemann problem at corners, Balsara [2] proposed the genuinely two-dimensional HLL Riemann solver. Unlike earlier multidimensional solvers, Balsara's solver is simple and easy to implement. Then, the genuinely two-dimensional HLL Riemann solver was extended to the unstructured mesh [7, 8, 14, 15, 18, 22]. Furthermore, Balsara et al. [4] developed a genuinely three-dimensional HLLE solver. Inspired by the work of Balsara, a series of effective genuinely two-dimensional HLL-type solvers have been constructed [17, 42, 48]. However, like 1D HLL solver, the genuinely multidimensional solvers derived from Balsara's method can not accurately capture shear waves. In order to overcome this defect, Balsara [3] constructed a genuinely two-dimensional HLLC solver, but this model is much complex and computationally expensive. Facing the challenge to construct an efficient two-dimensional solver with the capability of capturing contact discontinuities, Mandal and Sharma [40] introduced the convective-pressure splitting (CPS) strategy into the Balsara's 2D HLL solver to propose the genuinely multidimensional HLL-CPS solver. Since then, many contact-preserving genuinely multidimensional solvers based on convective-pressure flux splitting method [30,31,33] were developed. However, the solution dependent weighted least squares (SDWLS) method used to approximate the states of variables in these genuinely two-dimensional CPS solvers only provides second-order accuracy.

Unlike the SDWLS approach, the weighted essentially non-oscillatory (WENO) schemes [27,34,38,43,58] provide a strategy to obtain high-order accuracy. The WENO schemes are the developed versions of the essentially non-oscillatory (ENO) scheme. The original philosophy of the ENO scheme was first proposed by Harten et al. [28] and a more efficient finite difference form was developed by Shu and Osher [52,53]. The ENO method chooses the single one with the smallest variation from multiple stencils to reconstruct the values of variable in zone of interest. However, the use of a single stencil might result in a loss of accuracy. In order to overcome the shortcoming of ENO scheme, Liu et al. [38] and Jiang and Shu [34] proposed a fifth-order finite-difference weighted ENO (WENO) scheme, where the use of a nonlinear convex combination of lower order polynomials associated with each candidate stencil ensured the scheme achieving high-order accuracy in the smooth areas and capturing shock waves robustly in the discontinuous regions. Then, scholars have developed WENO schemes with higher order (over tenth-order accuracy) [1,9,13,25]. In 2016, Balsara et al. [10] proposed a very compact expression of reconstruction polynomials and the corresponding smoothness indicators using the Legendre basis. Since the calculation of smoothness indicators is expensive, the efficiency of finite difference WENO schemes is significantly improved due to the use of compact expression. Recently, Balsara et al. [6] presented a fourth-order divergence constraint-preserving prolongation strategy that is exact analytically. This is a practical extension of WENO schemes because some PDEs require that vector fields preserve a divergence constraint.

Due to the distinctive advantages of WENO schemes in stability and high accuracy, its application in the genuinely two-dimensional Riemann solvers has attracted much attention. Balsara and his collaborators [5,7,11,12,15] combined the high-order accuracy ADER-WENO scheme with the genuinely two-dimensional HLL Riemann solvers to solve the magnetohydrodynamics. The numerical results gave evidence of high accuracy of the schemes. Following Balsara's strategy, Zhou et al. [61] proposed two third-order reconstruction methods for the genuinely two-dimensional HLL solver. However, limited by the defects of genuinely two-dimensional HLL solver, these schemes exhibited a high dissipation behavior for contact waves.

The goal of the present work is to propose a simple fifth-order reconstruction method for the genuinely two-dimensional Riemann solver. For improving the resolution of contact waves, the genuinely multidimensional HLL-CPS solver [40] is employed to solve the Riemann problems. In order to obtain high accuracy, the fifth-order WENO scheme [34,51] is adopted to evaluate the values of conserved variables at the midpoint of interfaces and a simple dimension-by-dimension reconstruction consisting of a number of fifth-order sweeps [21,55] is employed to approximate states of conserved variables at corners. The paper is organized as follows. The governing equations and the Zha-Bilgen convection-pressure flux split formulation are reviewed in Section 2. The genuinely multidimensional HLL-CPS solver is presented in section 3 and the reconstruction procedures are detailedly described in Section 4. In Section 5, a series of test problems are calculated to exhibit performances of the proposed scheme. Finally, Section 6 summarizes our conclusions.

2 Governing equations

The two-dimensional inviscid compressible flow is considered here, and its governing equations can be given as

$$\partial_t \mathbf{U} + \partial_x \mathbf{F} + \partial_y \mathbf{G} = \mathbf{0}, \tag{2.1}$$

where

$$\mathbf{U} = \begin{bmatrix} \rho \\ \rho u \\ \rho v \\ E \end{bmatrix}, \quad \mathbf{F}(\mathbf{U}) = \begin{bmatrix} \rho u \\ \rho u^2 + p \\ \rho u v \\ u(E+p) \end{bmatrix}, \quad \mathbf{G}(\mathbf{U}) = \begin{bmatrix} \rho v \\ \rho u v \\ \rho v^2 + p \\ v(E+p) \end{bmatrix}. \tag{2.2}$$

Here, ρ represents density, u and v are velocities in two directions, E denotes total energy and p is pressure. The equation of state for ideal gas is considered here

$$p = (\gamma - 1)\left[E - \frac{1}{2}\rho\left(u^2 + v^2\right)\right], \tag{2.3}$$

where the specific heat ratio $\gamma = 1.4$.

We employ the finite volume method to discretize Eq. (2.1) on a Cartesian mesh. For a specific cell $\Omega_{i,j}$, the governing equations can be discretized as

$$\frac{d\mathbf{U}_{i,j}}{dt} = -\frac{\mathbf{F}_{i+\frac{1}{2},j} - \mathbf{F}_{i-\frac{1}{2},j}}{\Delta x} - \frac{\mathbf{G}_{i,j+\frac{1}{2}} - \mathbf{G}_{i,j-\frac{1}{2}}}{\Delta y}. \tag{2.4}$$

In (2.4), $\mathbf{U}_{i,j}$ is the average value of $\mathbf{U}$ on cell $\Omega_{i,j}$, Δx and Δy are space steps. To complete the design of the numerical method, the temporal discretization of Eq. (2.4) is performed by the third-order version of the Runge-Kutta scheme [50]

$$\begin{cases} \mathbf{U}^{(1)} = \mathbf{U}^n + \Delta t \mathbf{L}(\mathbf{U}^n), \\ \mathbf{U}^{(2)} = \dfrac{3}{4}\mathbf{U}^n + \dfrac{1}{4}\mathbf{U}^{(1)} + \dfrac{1}{4}\Delta t \mathbf{L}(\mathbf{U}^{(1)}), \\ \mathbf{U}^{n+1} = \dfrac{1}{3}\mathbf{U}^n + \dfrac{2}{3}\mathbf{U}^{(2)} + \dfrac{2}{3}\Delta t \mathbf{L}(\mathbf{U}^{(2)}), \end{cases} \tag{2.5}$$

where $\mathbf{L}(*)$ is the spatial operator, the superscripts n and $n+1$ denote the current and the subsequent time steps, and the superscripts (1) and (2) are the intermediate time-stages between them.

3 Genuinely two-dimensional HLL-CPS scheme

In the present work, the flux vectors are split into convective and pressure components with the Zha-Bilgen splitting formulation [60]

$$\mathbf{F}(\mathbf{U})=\mathbf{F}_1(\mathbf{U})+\mathbf{F}_2(\mathbf{U})=u\begin{bmatrix}\rho\\ \rho u\\ \rho v\\ E\end{bmatrix}+\begin{bmatrix}0\\ p\\ 0\\ pu\end{bmatrix}, \tag{3.1a}$$

$$\mathbf{G}(\mathbf{U})=\mathbf{G}_1(\mathbf{U})+\mathbf{G}_2(\mathbf{U})=v\begin{bmatrix}\rho\\ \rho u\\ \rho v\\ E\end{bmatrix}+\begin{bmatrix}0\\ 0\\ p\\ pv\end{bmatrix}. \tag{3.1b}$$

Here, $\mathbf{F}_1(\mathbf{U})$ and $\mathbf{G}_1(\mathbf{U})$ are convective parts of fluxes in the x and y-directions, $\mathbf{F}_2(\mathbf{U})$ and $\mathbf{G}_2(\mathbf{U})$ are pressure parts of fluxes.

Assuming the Euler equations are solved on a Cartesian mesh shown in Fig. 1(a) and considering the flux through interface $(i+\frac{1}{2},j)$, the genuinely multidimensional HLL-CPS scheme [40] not only solve the 1D Riemann problem at the midpoint $(i+\frac{1}{2},j)$ but also consider the 2D Riemann problem at corners $(i+\frac{1}{2},j+\frac{1}{2})$ and $(i+\frac{1}{2},j-\frac{1}{2})$. In the following two subsections, we briefly describe the genuinely multidimensional HLL-CPS scheme.

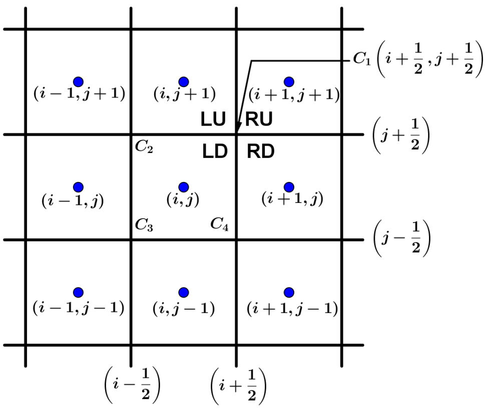

(a) The Cartesian mesh

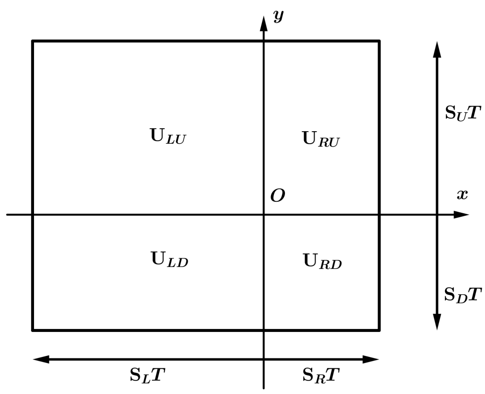

(b) The 2D Riemann problem at a corner

Figure 1: The Cartesian mesh and two-dimensional Riemann problem at a corner.

3.1 Evaluation of flux at the midpoint of a interface

We use $\mathbf{F}_1^{mid}$ and $\mathbf{F}_2^{mid}$ to represent the convective flux and the pressure flux at the midpoint of a interface. A method similar to the ASUM scheme [37] is employed to evaluate the convective numerical flux

$$\mathbf{F}_1^{mid} = M_k \begin{bmatrix} \rho \\ \rho u \\ \rho v \\ E \end{bmatrix}_k a_k, \quad k = \begin{cases} L, & \text{if } \bar{u} \geq 0, \\ R, & \text{if } \bar{u} < 0, \end{cases} \tag{3.2}$$

$\bar{u}$ is the average value of the local x-direction velocity $(u_L + u_R)/2$. The local Mach numbers and the sound velocities are calculated as

$$M_k = \begin{cases} \dfrac{\bar{u}}{\bar{u} - S_L^{mid}}, & \text{if } \bar{u} \geq 0, \\ \dfrac{\bar{u}}{\bar{u} - S_R^{mid}}, & \text{if } \bar{u} < 0, \end{cases} \qquad a_k = \begin{cases} u_L - S_L^{mid}, & \text{if } \bar{u} \geq 0, \\ u_R - S_R^{mid}, & \text{if } \bar{u} < 0. \end{cases} \tag{3.3}$$

The wave speeds of convective flux is evaluated as

$$S_L^{mid} = \min(0, u_L - a_L, \tilde{u}_L - \tilde{a}_L), \quad S_R^{mid} = \max(0, u_R + a_R, \tilde{u}_R + \tilde{a}_R). \tag{3.4}$$

The pressure part of flux vector is calculated by

$$\mathbf{F}_2^{mid} = \frac{1}{2}(\mathbf{F}_{2L} + \mathbf{F}_{2R}) + \Delta \mathbf{U}_2, \tag{3.5}$$

where fluxes $\mathbf{F}_{2L}$ and $\mathbf{F}_{2R}$ are evaluated through left and right states, respectively. According to the isentropic assumption, the numerical diffusion term $\Delta\mathbf{U}_2$ is given as

$$\Delta \mathbf{U}_2 = \frac{S_R^{mid} + S_L^{mid}}{2(S_R^{mid} - S_L^{mid})} (\mathbf{F}_{2L} - \mathbf{F}_{2R}) - \frac{S_R^{mid} S_L^{mid}}{\bar{a}^2 (S_R^{mid} - S_L^{mid})} \begin{bmatrix} p_L - p_R \\ (pu)_L - (pu)_R \\ (pv)_L - (pv)_R \\ E_L^* - E_R^* \end{bmatrix}, \tag{3.6}$$

where the average value of speed of sound is given as $\bar{a} = (a_L + a_R)/2$ and E_k^* is calculated by

$$E_k^* = \frac{\bar{a}^2}{\gamma - 1} p_k + \frac{1}{2} p_k (u_k^2 + v_k^2), \quad k = L, R.$$

3.2 Evaluation of two-dimensional flux at corners

As shown in Fig. 1(b), the two-dimensional Riemann problem at the corner C_1 $(i+\frac{1}{2}, j+\frac{1}{2})$ involves four different states, namely $\mathbf{U}_{LD}$, $\mathbf{U}_{LU}$, $\mathbf{U}_{RD}$ and $\mathbf{U}_{RU}$. The genuinely multidimensional HLL-CPS scheme [40] is adopted to solve the two-dimensional Riemann problem. We use $\mathbf{F}_1^{cor}$ and $\mathbf{G}_1^{cor}$ to denote the convective fluxes in the x- and y-directions at the corner $(i+\frac{1}{2}, j+\frac{1}{2})$ and use $\mathbf{F}_2^{cor}$ and $\mathbf{G}_2^{cor}$ to denote the pressure fluxes. In the following part of this subsection, we will briefly describe the evaluation of convective and pressure fluxes at the corner $(i+\frac{1}{2},j+\frac{1}{2})$.

The x-directional convective flux at the corner C_1 is calculated as

$$\mathbf{F}_1^{cor}=\frac{\bar{u}}{S_U-S_D}\left(S_U\begin{bmatrix}\rho\\\rho u\\\rho v\\E\end{bmatrix}_{k1}-S_D\begin{bmatrix}\rho\\\rho u\\\rho v\\E\end{bmatrix}_{k2}\right),\quad \begin{cases}k_1=LU,\quad k_2=LD,\quad \text{if }\bar{u}\geq 0,\\ k_1=RU,\quad k_2=RD,\quad \text{if }\bar{u}<0.\end{cases} \tag{3.7}$$

The averaged value of $x-$directional velocities at corner C_1 is given as

$$\bar{u}=\frac{u_{LU}S_U-u_{LD}S_D+u_{RU}S_U-u_{RD}S_D}{2(S_U-S_D)}.$$

Similarly, the y-directional convective flux at the corner is evaluated as

$$\mathbf{G}_1^{cor}=\frac{\bar{v}}{S_R-S_L}\left(S_R\begin{bmatrix}\rho\\\rho u\\\rho v\\E\end{bmatrix}_{k_1}-S_L\begin{bmatrix}\rho\\\rho u\\\rho v\\E\end{bmatrix}_{k_2}\right),\quad \begin{cases}k_1=RD,\quad k_2=LD,\quad \text{if }\bar{v}\geq 0,\\ k_1=RU,\quad k_2=LU,\quad \text{if }\bar{v}<0.\end{cases} \tag{3.8}$$

The averaged value of $y-$directional velocity at corner C_1 is defined as

$$\bar{v}=\frac{v_{RU}S_R-v_{LU}S_L+v_{RD}S_R-v_{LD}S_L}{2(S_R-S_L)}.$$

At the corner $C_1(i+\frac{1}{2},j+\frac{1}{2})$, the two-dimensional pressure flux is calculated as [40]

$$\mathbf{F}_2^{cor}=\frac{1}{2}(\hat{\mathbf{F}}_{2L}+\hat{\mathbf{F}}_{2R})+\Delta\mathbf{U}_{2x}-\frac{2S_RS_L(\mathbf{G}_{2RU}-\mathbf{G}_{2LU}+\mathbf{G}_{2LD}-\mathbf{G}_{2RD})}{(S_R-S_L)(S_U-S_D)}, \tag{3.9a}$$

$$\mathbf{G}_2^{cor}=\frac{1}{2}(\hat{\mathbf{G}}_{2D}+\hat{\mathbf{G}}_{2U})+\Delta\mathbf{U}_{2y}-\frac{2S_US_D(\mathbf{F}_{2RU}-\mathbf{F}_{2LU}+\mathbf{F}_{2LD}-\mathbf{F}_{2RD})}{(S_R-S_L)(S_U-S_D)}, \tag{3.9b}$$

where

$$\hat{\mathbf{F}}_{2L}=\frac{\mathbf{F}_{2LU}S_U-\mathbf{F}_{2LD}S_D}{S_U-S_D},\qquad \hat{\mathbf{F}}_{2R}=\frac{\mathbf{F}_{2RU}S_U-\mathbf{F}_{2RD}S_D}{S_U-S_D},$$

$$\hat{\mathbf{G}}_{2D}=\frac{\mathbf{G}_{2RD}S_R-\mathbf{G}_{2LD}S_R}{S_R-S_L},\qquad \hat{\mathbf{G}}_{2U}=\frac{\mathbf{G}_{2RU}S_R-\mathbf{G}_{2LU}S_R}{S_R-S_L}.$$

According to the isentropic condition, the expressions of the numerical diffusion terms in Eqs. (3.9a) and (3.9b) are given as

$$\Delta\mathbf{U}_{2x}=\frac{S_R+S_L}{2(S_R-S_L)}(\hat{\mathbf{F}}_{2L}-\hat{\mathbf{F}}_{2R})$$
$$+\frac{S_RS_L\begin{bmatrix} S_U(p_{RU}-p_{LU})-S_D(p_{RD}-p_{LD}) \\ S_U[(pu)_{RU}-(pu)_{LU}]-S_D[(pu)_{RD}-(pu)_{LD}] \\ S_U[(pv)_{RU}-(pv)_{LU}]-S_D[(pv)_{RD}-(pv)_{LD}] \\ S_U(E^*_{RU}-E^*_{LU})-S_D(E^*_{RD}-E^*_{LD}) \end{bmatrix}}{\bar{a}^2(S_R-S_L)(S_U-S_D)}, \tag{3.10a}$$

$$\Delta\mathbf{U}_{2y}=\frac{S_U+S_D}{2(S_U-S_D)}\ (\hat{\mathbf{G}}_{2D}-\hat{\mathbf{G}}_{2U})$$
$$+\frac{S_US_D\begin{bmatrix} S_R(p_{RU}-p_{RD})-S_L(p_{LU}-p_{LD}) \\ S_R[(pu)_{RU}-(pu)_{RD}]-S_L[(pu)_{LU}-(pu)_{LD}] \\ S_R[(pv)_{RU}-(pv)_{RD}]-S_L[(pv)_{LU}-(pv)_{LD}] \\ S_R(E^*_{RU}-E^*_{RD})-S_L(E^*_{LU}-E^*_{LD}) \end{bmatrix}}{\bar{a}^2\ (S_R-S_L)(S_U-S_D)}, \tag{3.10b}$$

where the average sound velocity $\bar{a}$ and the total energy E^*_k are respectively defined as

$$\bar{a}=\frac{a_{LD}+a_{LU}+a_{RD}+a_{RU}}{4},\quad E^*_k=\frac{\bar{a}^2}{\gamma-1}p_k+\frac{1}{2}p_k\ (u_k^2+v_k^2),$$
$$k=LU,\ RU,\ LD,\ RD.$$

The wave speeds travelling along four directions at the corner are evaluated as

$$\begin{cases} S_L=\min(0,\ \lambda_x^0(\mathbf{U}_{LU}),\ \lambda_x^0(\mathbf{U}_{LD}),\ \tilde{\lambda}_x^0(\mathbf{U}_{LU},\mathbf{U}_{RU}),\ \tilde{\lambda}_x^0(\mathbf{U}_{LD},\mathbf{U}_{RD})), \\ S_R=\max(0,\ \lambda_x^1(\mathbf{U}_{RU}),\ \lambda_x^1(\mathbf{U}_{RD}),\ \tilde{\lambda}_x^1(\mathbf{U}_{LU},\mathbf{U}_{RU}),\ \tilde{\lambda}_x^1(\mathbf{U}_{LD},\mathbf{U}_{RD})), \\ S_D=\min(0,\ \lambda_y^0(\mathbf{U}_{RD}),\ \lambda_y^0(\mathbf{U}_{LD}),\ \tilde{\lambda}_y^0(\mathbf{U}_{RD},\mathbf{U}_{RU}),\ \tilde{\lambda}_y^0(\mathbf{U}_{LD},\mathbf{U}_{LU})), \\ S_U=\max(0,\ \lambda_y^1(\mathbf{U}_{RU}),\ \lambda_y^1(\mathbf{U}_{LU}),\ \tilde{\lambda}_y^1(\mathbf{U}_{RD},\mathbf{U}_{RU}),\ \tilde{\lambda}_y^1(\mathbf{U}_{LD},\mathbf{U}_{LU})), \end{cases} \tag{3.11}$$

where $\lambda_x^0(\mathbf{U}_{LU})$ is the minimum x-directional wave speed in the state $\mathbf{U}_{LU}$, $\lambda_x^1(\mathbf{U}_{LU})$ is the maximum x-directional wave speed in the state $\mathbf{U}_{LU}$, $\tilde{\lambda}_x^0$ $(\mathbf{U}_{LU},\ \mathbf{U}_{RU})$ is the Roe's averaged value of the minimum x-direction wave speed between states $\mathbf{U}_{LU}$ and $\mathbf{U}_{RU}$, $\tilde{\lambda}_x^1$ $(\mathbf{U}_{LU},\mathbf{U}_{RU})$ is the Roe's averaged value of the maximum x-direction wave speed between states $\mathbf{U}_{LU}$ and $\mathbf{U}_{RU}$.

3.3 Evaluation of total flux through an interface

As illustrated in Fig. 1(a), the two-dimensional fluxes at corners C_1 $(i+\frac{1}{2},j+\frac{1}{2})$ and C_4 $(i+\frac{1}{2},j-\frac{1}{2})$ and the flux at the midpoint $(i+\frac{1}{2},j)$ constitute the total x-directional flux through the interface $(i+\frac{1}{2},j)$. The Simpson's integral formula is adopted to assemble these fluxes to obtain the total flux

$$\mathbf{F}_{i+\frac{1}{2},j}=\frac{1}{6}\mathbf{F}^{cor}_{i+\frac{1}{2},j+\frac{1}{2}}+\frac{4}{6}\mathbf{F}^{mid}_{i+\frac{1}{2},j}+\frac{1}{6}\mathbf{F}^{cor}_{i+\frac{1}{2},j-\frac{1}{2}}. \tag{3.12}$$

4 Fifth-order reconstruction method

In this paper, a fifth-order method consisting of a number of WENO sweeps is employed to approximate the values of conservative variables vector. Some researches have reported that to reconstruct conservative variables may introduce spurious oscillations near material interfaces [21, 55]. Therefore, the one-dimensional WENO sweep in the x-direction is always performed on characteristic fields defined by $\mathbf{A}^{\mathbf{F}}=\partial\mathbf{F}/\partial\mathbf{U}$, while the one-dimensional WENO sweep in the y-direction is carried out on characteristic fields defined by $\mathbf{A}^{\mathbf{G}}=\partial\mathbf{G}/\partial\mathbf{U}$ in this work.

For the convenience of reader, we give a brief explanation of the symbols used in this section. $\mathbf{W}$ is the vector of characteristic variables. $\mathbf{L}$ and $\mathbf{R}$ are the left and right characteristic matrices, respectively. Superscript $\mathbf{F}$ (or $\mathbf{G}$) of a variable denotes it is relevant with $\mathbf{A}^{\mathbf{F}}$ (or $\mathbf{A}^{\mathbf{G}}$). Superscripts L,R, D and U respectively denote the 'left', 'right', 'down' and 'up' states of variables. Similarly, LD,LU,RD and RU represent the 'left-down', 'left-up', 'right-down' and 'right-up' states of variables at a corner (see Fig. 1). In addition, subscript (i,j) indicates a variable is defined at the center of cell, and subscripts $(i+\frac{1}{2},j)$ and $(i+\frac{1}{2},j+\frac{1}{2})$ respectively indicate the variables are defined at mid-point and corner of interface.

4.1 The reconstruction of conserved variables vectors at midpoint

In order to implement reconstruction on local characteristic fields, the conservative variables at six cells near interface $(i+\frac{1}{2},j)$ are projected onto characteristic fields

$$\mathbf{W}^{\mathbf{F}}_{k,j}=\mathbf{L}^{\mathbf{F}}_{i+\frac{1}{2},j}\mathbf{U}_{k,j},\quad k=i-2,\dots,i+3, \tag{4.1}$$

where $\mathbf{L}^{\mathbf{F}}_{i+1/2,j}$ is the local left characteristic matrix of $\mathbf{A}^{\mathbf{F}}$ and it is evaluated through $\mathbf{U}_{i+1/2,j}=(\mathbf{U}_{i,j}+\mathbf{U}_{i+1,j})/2$. Three stencils are arranged as

$$s_{(0)}=\left\{\mathbf{W}^{\mathbf{F}}_{i,j},\mathbf{W}^{\mathbf{F}}_{i+1,j},\mathbf{W}^{\mathbf{F}}_{i+2,j}\right\}, \tag{4.2a}$$

$$s_{(1)}=\left\{\mathbf{W}^{\mathbf{F}}_{i-1,j},\mathbf{W}^{\mathbf{F}}_{i,j},\mathbf{W}^{\mathbf{F}}_{i+1,j}\right\}, \tag{4.2b}$$

$$s_{(2)}=\left\{\mathbf{W}^{\mathbf{F}}_{i-2,j},\mathbf{W}^{\mathbf{F}}_{i-1,j},\mathbf{W}^{\mathbf{F}}_{i,j}\right\}. \tag{4.2c}$$

The smooth indicators of these stencils are calculated as

$$\left\{\begin{aligned}
\beta^{(0)}&=\frac{13}{12}\left(\mathbf{W}^{\mathbf{F}}_{i,j}-2\mathbf{W}^{\mathbf{F}}_{i+1,j}+\mathbf{W}^{\mathbf{F}}_{i+2,j}\right)^2+\frac{1}{4}\left(3\mathbf{W}^{\mathbf{F}}_{i,j}-4\mathbf{W}^{\mathbf{F}}_{i+1,j}+\mathbf{W}^{\mathbf{F}}_{i+2,j}\right)^2,\\
\beta^{(1)}&=\frac{13}{12}\left(\mathbf{W}^{\mathbf{F}}_{i-1,j}-2\mathbf{W}^{\mathbf{F}}_{i,j}+\mathbf{W}^{\mathbf{F}}_{i+1,j}\right)^2+\frac{1}{4}\left(\mathbf{W}^{\mathbf{F}}_{i-1,j}-\mathbf{W}^{\mathbf{F}}_{i+1,j}\right)^2,\\
\beta^{(2)}&=\frac{13}{12}\left(\mathbf{W}^{\mathbf{F}}_{i-2,j}-2\mathbf{W}^{\mathbf{F}}_{i-1,j}+\mathbf{W}^{\mathbf{F}}_{i,j}\right)^2+\frac{1}{4}\left(\mathbf{W}^{\mathbf{F}}_{i-2,j}-4\mathbf{W}^{\mathbf{F}}_{i-1,j}+3\mathbf{W}^{\mathbf{F}}_{i,j}\right)^2.
\end{aligned}\right. \tag{4.3}$$

For the fifth order WENO scheme [51], the ideal weights for the left states at interface $(i+\frac{1}{2},j)$ are given as

$$d^{(0)}=\frac{3}{10}, \quad d^{(1)}=\frac{3}{5}, \quad d^{(2)}=\frac{1}{10}. \tag{4.4}$$

With the definition of nonlinear weights

$$\alpha^{(r)}=\frac{d^{(r)}}{(\beta^{(r)}+\epsilon)^2}, \quad \omega^{(r)}=\frac{\alpha^{(r)}}{\sum_{s=0}^{2}\alpha^{(s)}}, \quad r=0,1,2, \tag{4.5}$$

the left states of characteristic variables at interface $(i+\frac{1}{2},j)$ are approximated as

$$\begin{aligned}\mathbf{W}^{(L),\mathbf{F}}_{i+\frac{1}{2},j}=&\omega^{(0)}\left(\frac{1}{3}\mathbf{W}^{\mathbf{F}}_{i,j}+\frac{5}{6}\mathbf{W}^{\mathbf{F}}_{i+1,j}-\frac{1}{6}\mathbf{W}^{\mathbf{F}}_{i+2,j}\right)\\&+\omega^{(1)}\left(-\frac{1}{6}\mathbf{W}^{\mathbf{F}}_{i-1,j}+\frac{5}{6}\mathbf{W}^{\mathbf{F}}_{i,j}+\frac{1}{3}\mathbf{W}^{\mathbf{F}}_{i+1,j}\right)\\&+\omega^{(2)}\left(\frac{1}{3}\mathbf{W}^{\mathbf{F}}_{i-2,j}-\frac{7}{6}\mathbf{W}^{\mathbf{F}}_{i-1,j}+\frac{11}{6}\mathbf{W}^{\mathbf{F}}_{i,j}\right).\end{aligned} \tag{4.6}$$

The stencils for obtaining the right state of characteristic variables at interface $(i+\frac{1}{2},j)$ are arranged as

$$s_{(0)}=\left\{\mathbf{W}^{\mathbf{F}}_{i+1,j},\mathbf{W}^{\mathbf{F}}_{i+2,j},\mathbf{W}^{\mathbf{F}}_{i+3,j}\right\}, \tag{4.7a}$$
$$s_{(1)}=\left\{\mathbf{W}^{\mathbf{F}}_{i,j},\mathbf{W}^{\mathbf{F}}_{i+1,j},\mathbf{W}^{\mathbf{F}}_{i+2,j}\right\}, \tag{4.7b}$$
$$s_{(2)}=\left\{\mathbf{W}^{\mathbf{F}}_{i-1,j},\mathbf{W}^{\mathbf{F}}_{i,j},\mathbf{W}^{\mathbf{F}}_{i+1,j}\right\}. \tag{4.7c}$$

Three smooth factors are calculated as

$$\left\{\begin{aligned}\beta^{(0)}&=\frac{13}{12}\left(\mathbf{W}^{\mathbf{F}}_{i+1,j}-2\mathbf{W}^{\mathbf{F}}_{i+2,j}+\mathbf{W}^{\mathbf{F}}_{i+3,j}\right)^2+\frac{1}{4}\left(3\mathbf{W}^{\mathbf{F}}_{i+1,j}-4\mathbf{W}^{\mathbf{F}}_{i+2,j}+\mathbf{W}^{\mathbf{F}}_{i+3,j}\right)^2,\\\beta^{(1)}&=\frac{13}{12}\left(\mathbf{W}^{\mathbf{F}}_{i,j}-2\mathbf{W}^{\mathbf{F}}_{i+1,j}+\mathbf{W}^{\mathbf{F}}_{i,j}\right)^2+\frac{1}{4}\left(\mathbf{W}^{\mathbf{F}}_{i,j}-\mathbf{W}^{\mathbf{F}}_{i+2,j}\right)^2,\\\beta^{(2)}&=\frac{13}{12}\left(\mathbf{W}^{\mathbf{F}}_{i-1,j}-2\mathbf{W}^{\mathbf{F}}_{i,j}+\mathbf{W}^{\mathbf{F}}_{i+1,j}\right)^2+\frac{1}{4}\left(\mathbf{W}^{\mathbf{F}}_{i-1,j}-4\mathbf{W}^{\mathbf{F}}_{i,j}+3\mathbf{W}^{\mathbf{F}}_{i+1,j}\right)^2.\end{aligned}\right. \tag{4.8}$$

The ideal weights are evaluated as

$$d^{(0)}=\frac{1}{10}, \quad d^{(1)}=\frac{3}{5}, \quad d^{(2)}=\frac{3}{10}. \tag{4.9}$$

Evaluating nonlinear weights through Eq. (4.5), then, the right states of characteristic variables at interface $(i+\frac{1}{2},j)$ are given as

$$\begin{aligned}\mathbf{W}^{(R),\mathbf{F}}_{i+\frac{1}{2},j}=&\omega^{(0)}\left(\frac{11}{6}\mathbf{W}^{\mathbf{F}}_{i+1,j}-\frac{7}{6}\mathbf{W}^{\mathbf{F}}_{i+2,j}+\frac{1}{3}\mathbf{W}^{\mathbf{F}}_{i+3,j}\right)\\&+\omega^{(1)}\left(\frac{1}{3}\mathbf{W}^{\mathbf{F}}_{i,j}+\frac{5}{6}\mathbf{W}^{\mathbf{F}}_{i+1,j}-\frac{1}{6}\mathbf{W}^{\mathbf{F}}_{i+2,j}\right)\\&+\omega^{(2)}\left(-\frac{1}{6}\mathbf{W}^{\mathbf{F}}_{i-1,j}+\frac{5}{6}\mathbf{W}^{\mathbf{F}}_{i,j}+\frac{1}{3}\mathbf{W}^{\mathbf{F}}_{i+1,j}\right).\end{aligned}\tag{4.10}$$

Once the left and right states of characteristic variables at the midpoint of interface $(i+\frac{1}{2},j)$ are obtained, the left and right states of conserved variables vector are evaluated as

$$\mathbf{U}^{*}_{i+\frac{1}{2},j}=\mathbf{R}^{\mathbf{F}}_{i+\frac{1}{2},j}\mathbf{W}^{(*),\mathbf{F}}_{i+\frac{1}{2},j},\quad *=L,R.\tag{4.11}$$

In order to obtain up and down states of the characteristic variables at interface $(i,j+\frac{1}{2})$, the conservative variables are projected onto the local characteristic fields

$$\mathbf{W}^{\mathbf{G}}_{i,h}=\mathbf{L}^{\mathbf{G}}_{i,j+\frac{1}{2}}\mathbf{U}_{i,h},\quad h=j-2,\cdots,j+3,\tag{4.12}$$

Three stencils for the reconstruction of down states of characteristic variables at interface $(i,j+\frac{1}{2})$ are formed as

$$s_{(0)}=\left\{\mathbf{W}^{\mathbf{G}}_{i,j},\mathbf{W}^{\mathbf{G}}_{i,j+1},\mathbf{W}^{\mathbf{G}}_{i,j+2}\right\},\tag{4.13a}$$

$$s_{(1)}=\left\{\mathbf{W}^{\mathbf{G}}_{i,j-1},\mathbf{W}^{\mathbf{G}}_{i,j},\mathbf{W}^{\mathbf{G}}_{i,j+1}\right\},\tag{4.13b}$$

$$s_{(2)}=\left\{\mathbf{W}^{\mathbf{G}}_{i,j-2},\mathbf{W}^{\mathbf{G}}_{i,j-1},\mathbf{W}^{\mathbf{G}}_{i,j}\right\}.\tag{4.13c}$$

The smooth indicators are calculated as

$$\left\{\begin{aligned}\beta^{(0)}&=\frac{13}{12}\left(\mathbf{W}^{\mathbf{G}}_{i,j}-2\mathbf{W}^{\mathbf{G}}_{i,j+1}+\mathbf{W}^{\mathbf{G}}_{i,j+2}\right)^2+\frac{1}{4}\left(3\mathbf{W}^{\mathbf{G}}_{i,j}-4\mathbf{W}^{\mathbf{G}}_{i,j+1}+\mathbf{W}^{\mathbf{G}}_{i,j+2}\right)^2,\\\beta^{(1)}&=\frac{13}{12}\left(\mathbf{W}^{\mathbf{G}}_{i,j-1}-2\mathbf{W}^{\mathbf{G}}_{i,j}+\mathbf{W}^{\mathbf{G}}_{i,j+1}\right)^2+\frac{1}{4}\left(\mathbf{W}^{\mathbf{G}}_{i,j-1}-\mathbf{W}^{\mathbf{G}}_{i,j+1}\right)^2,\\\beta^{(2)}&=\frac{13}{12}\left(\mathbf{W}^{\mathbf{G}}_{i,j-2}-2\mathbf{W}^{\mathbf{G}}_{i,j-1}+\mathbf{W}^{\mathbf{G}}_{i,j}\right)^2+\frac{1}{4}\left(\mathbf{W}^{\mathbf{G}}_{i,j-2}-4\mathbf{W}^{\mathbf{G}}_{i,j-1}+3\mathbf{W}^{\mathbf{G}}_{i,j}\right)^2.\end{aligned}\right.\tag{4.14}$$

The nonlinear weights are evaluated using Eq. (4.5), then, the down states of characteristic variables at interface $(i,j+\frac{1}{2})$ are obtained as

$$\begin{aligned}\mathbf{W}^{(D),\mathbf{G}}_{i,j+\frac{1}{2}}=&\omega^{(0)}\left(\frac{1}{3}\mathbf{W}^{\mathbf{G}}_{i,j}+\frac{5}{6}\mathbf{W}^{\mathbf{G}}_{i,j+1}-\frac{1}{6}\mathbf{W}^{\mathbf{G}}_{i,j+2}\right)\\&+\omega^{(1)}\left(-\frac{1}{6}\mathbf{W}^{\mathbf{G}}_{i,j-1}+\frac{5}{6}\mathbf{W}^{\mathbf{G}}_{i,j}+\frac{1}{3}\mathbf{W}^{\mathbf{G}}_{i,j+1}\right)\\&+\omega^{(2)}\left(\frac{1}{3}\mathbf{W}^{\mathbf{G}}_{i,j-2}-\frac{7}{6}\mathbf{W}^{\mathbf{G}}_{i,j-1}+\frac{11}{6}\mathbf{W}^{\mathbf{G}}_{i,j}\right).\end{aligned}\tag{4.15}$$

Similarly, the up states of characteristic variables at interface $(i,j+\frac{1}{2})$ are approximated as

$$\begin{aligned}\mathbf{W}^{(U),\mathbf{G}}_{i,j+\frac{1}{2}}=&\omega^{(0)}\left(\frac{11}{6}\mathbf{W}^{\mathbf{G}}_{i,j+1}-\frac{7}{6}\mathbf{W}^{\mathbf{G}}_{i,j+2}+\frac{1}{3}\mathbf{W}^{\mathbf{G}}_{i,j+3}\right)\\&+\omega^{(1)}\left(\frac{1}{3}\mathbf{W}^{\mathbf{G}}_{i,j}+\frac{5}{6}\mathbf{W}^{\mathbf{G}}_{i,j+1}-\frac{1}{6}\mathbf{W}^{\mathbf{G}}_{i,j+2}\right)\\&+\omega^{(2)}\left(-\frac{1}{6}\mathbf{W}^{\mathbf{G}}_{i,j-1}+\frac{5}{6}\mathbf{W}^{\mathbf{G}}_{i,j}+\frac{1}{3}\mathbf{W}^{\mathbf{G}}_{i,j+1}\right).\end{aligned}\tag{4.16}$$

Then, the down and up states of conserved variables vector at interface $(i,j+\frac{1}{2})$ are obtained as

$$\mathbf{U}^{*}_{i,j+\frac{1}{2}}=\mathbf{R}^{\mathbf{G}}_{i,j+\frac{1}{2}}\mathbf{W}^{(*),\mathbf{G}}_{i,j+\frac{1}{2}},\quad *=U,D.\tag{4.17}$$

It should be noted that the reconstruction of characteristic variables on different interfaces is independent of each other. In the procedure to reconstruct variables at an interface, same left and right characteristic matrices defined at this interface are adopted to calculate characteristic variables in near six cells. For instance, $\mathbf{L}^{\mathbf{F}}_{i+1/2,j}$ in Eq. (4.1) is defined at interface $(i+\frac{1}{2},j)$ and it is evaluated through $\mathbf{U}_{i+1/2,j}=(\mathbf{U}_{i,j}+\mathbf{U}_{i+1,j})/2$. In addition, $\mathbf{R}^{\mathbf{F}}_{i+1/2,j}$ in Eq. (4.11) is still defined at the interface $(i+\frac{1}{2},j)$.

4.2 The reconstruction of conserved variables vectors at corner

A dimension-by-dimension WENO reconstruction method consisting of a number of one-dimensional WENO sweeps in x and y-direction is adopted to calculate four states of conserved variable vectors at corners. Now, we give the approximate procedure to obtain the values of conserved variable vectors at corner C_1 $(i+\frac{1}{2},j+\frac{1}{2})$ shown in Fig. 1.

The dimension-by-dimension reconstruction is a two-step process. In the first step, twelve one-dimensional WENO sweeps in x-direction are carried out to approximate the left and right states of characteristic variables at interface $(i+\frac{1}{2},h)$, $h=j-2,\cdots,j+3$. As illustrated in Fig. 2, the characteristic variables in 36 cells around the corner C_1 are calculated through projecting the conservative variables onto characteristic fields

$$\mathbf{W}^{\mathbf{F}}_{k,h}=\mathbf{L}^{\mathbf{F}}_{i+\frac{1}{2},j+\frac{1}{2}}\mathbf{U}_{k,h},\quad k=i-2,\ldots,i+3,\quad h=j-2,\ldots,j+3,\tag{4.18}$$

where $\mathbf{L}^{\mathbf{F}}_{i+1/2,j+1/2}$ is the left characteristic matrix defined by $\mathbf{A}^{\mathbf{F}}$ at corner C_1. Then, the left and right states of characteristic variables at six interfaces $(i+\frac{1}{2},h)$, $h=j-2,\cdots,j+3$ are obtained through performing the one-dimensional WENO reconstruction in x-direction. For instance, after forming the stencils like Eq. (4.2) (as shown in Fig. 2) with $\mathbf{W}^{\mathbf{F}}_{k,j+1}$, $k=i-2,\ldots,i+2$ and calculating smooth indicators as Eq. (4.3) and nonlinear weights as

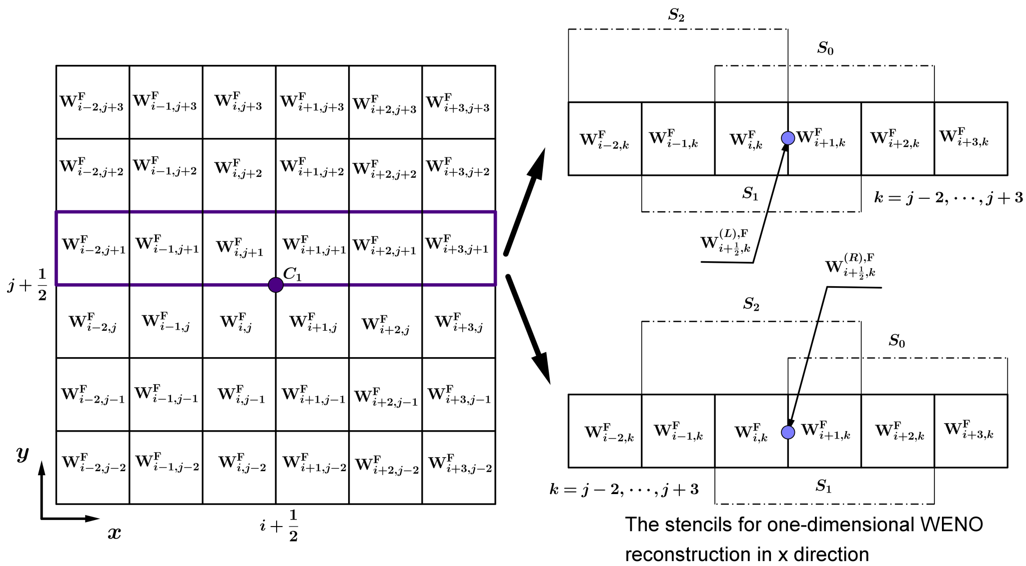

Figure 2: Illustration of the characteristic variables in 36 cells and the stencils of one-dimensional WENO reconstruction in x direction used in the first step of dimensional-by-dimensional reconstruction.

Eq. (4.4), the left states of characteristic variables at interface $(i+\frac{1}{2},j+1)$ are given as

$$\begin{aligned}\mathbf{W}^{(L),\mathbf{F}}_{i+\frac{1}{2},j+1}=&\omega^{(0)}\left(\frac{1}{3}\mathbf{W}^{\mathbf{F}}_{i,j+1}+\frac{5}{6}\mathbf{W}^{\mathbf{F}}_{i+1,j+1}-\frac{1}{6}\mathbf{W}^{\mathbf{F}}_{i+2,j+1}\right)\\&+\omega^{(1)}\left(-\frac{1}{6}\mathbf{W}^{\mathbf{F}}_{i-1,j+1}+\frac{5}{6}\mathbf{W}^{\mathbf{F}}_{i,j+1}+\frac{1}{3}\mathbf{W}^{\mathbf{F}}_{i+1,j+1}\right)\\&+\omega^{(2)}\left(\frac{1}{3}\mathbf{W}^{\mathbf{F}}_{i-2,j+1}-\frac{7}{6}\mathbf{W}^{\mathbf{F}}_{i-1,j+1}+\frac{11}{6}\mathbf{W}^{\mathbf{F}}_{i,j+1}\right).\end{aligned}\tag{4.19}$$

Similarly, following the procedure of Eq. (4.7c) to (4.10), the right states of characteristic variables at interface $(i+\frac{1}{2},j+1)$ are calculated as

$$\begin{aligned}\mathbf{W}^{(R),\mathbf{F}}_{i+\frac{1}{2},j+1}=&\omega^{(0)}\left(\frac{11}{6}\mathbf{W}^{\mathbf{F}}_{i+1,j+1}-\frac{7}{6}\mathbf{W}^{\mathbf{F}}_{i+2,j+1}+\frac{1}{3}\mathbf{W}^{\mathbf{F}}_{i+3,j+1}\right)\\&+\omega^{(1)}\left(\frac{1}{3}\mathbf{W}^{\mathbf{F}}_{i,j+1}+\frac{5}{6}\mathbf{W}^{\mathbf{F}}_{i+1,j+1}-\frac{1}{6}\mathbf{W}^{\mathbf{F}}_{i+2,j+1}\right)\\&+\omega^{(2)}\left(-\frac{1}{6}\mathbf{W}^{\mathbf{F}}_{i-1,j+1}+\frac{5}{6}\mathbf{W}^{\mathbf{F}}_{i,j+1}+\frac{1}{3}\mathbf{W}^{\mathbf{F}}_{i+1,j+1}\right).\end{aligned}\tag{4.20}$$

In the second step, the four states of characteristic variables at corner C_1 are calculated. Because one-dimensional WENO reconstructions in y-direction are carried out on the characteristic fields defined by $\mathbf{A}^{\mathbf{G}}$, the left and right states of characteristic variables defined by $\mathbf{A}^{\mathbf{G}}$ need to be obtained through following two step

$$\mathbf{U}^{(*)}_{i+\frac{1}{2},h}=\mathbf{R}^{\mathbf{F}}_{i+\frac{1}{2},j+\frac{1}{2}}\mathbf{W}^{(*),\mathbf{F}}_{i+\frac{1}{2},h},\quad \mathbf{W}^{(*),\mathbf{G}}_{i+\frac{1}{2},h}=\mathbf{L}^{\mathbf{G}}_{i+\frac{1}{2},j+\frac{1}{2}}\mathbf{U}^{(*)}_{i+\frac{1}{2},h},\quad h=j-2,\dots,j+3. \tag{4.21}$$

Here, $(*)=(L),(R)$. As illustrated in Fig. 3, stencils for one-dimensional WENO sweep in y-direction are arranged like Eq. (4.13), and smooth indicators and nonlinear weights are respectively evaluated as Eq. (4.3) and Eq. (4.5). Then, the down states of characteristic variables at corner C_1 are obtained as

$$\begin{aligned}\mathbf{W}^{(*D),\mathbf{G}}_{i+\frac{1}{2},j+\frac{1}{2}}=&\omega^{(0)}\left(\frac{1}{3}\mathbf{W}^{(*),\mathbf{G}}_{i+\frac{1}{2},j}+\frac{5}{6}\mathbf{W}^{(*),\mathbf{G}}_{i+\frac{1}{2},j+1}-\frac{1}{6}\mathbf{W}^{(*),\mathbf{G}}_{i+\frac{1}{2},j+2}\right)\\&+\omega^{(1)}\left(-\frac{1}{6}\mathbf{W}^{(*),\mathbf{G}}_{i+\frac{1}{2},j-1}+\frac{5}{6}\mathbf{W}^{(*),\mathbf{G}}_{i+\frac{1}{2},j}+\frac{1}{3}\mathbf{W}^{(*),\mathbf{G}}_{i+\frac{1}{2},j+1}\right)\\&+\omega^{(2)}\left(\frac{1}{3}\mathbf{W}^{(*),\mathbf{G}}_{i+\frac{1}{2},j-2}-\frac{7}{6}\mathbf{W}^{(*),\mathbf{G}}_{i+\frac{1}{2},j-1}+\frac{11}{6}\mathbf{W}^{(*),\mathbf{G}}_{i+\frac{1}{2},j}\right),\end{aligned} \tag{4.22}$$

where $(*D)=(LD),(RD)$. Similarly, the up states of characteristic variables at corner C_1 are approximated as

$$\begin{aligned}\mathbf{W}^{(*U),\mathbf{G}}_{i+\frac{1}{2},j+\frac{1}{2}}=&\omega^{(0)}\left(\frac{11}{6}\mathbf{W}^{(*),\mathbf{G}}_{i+\frac{1}{2},j+1}-\frac{7}{6}\mathbf{W}^{(*),\mathbf{G}}_{i+\frac{1}{2},j+2}+\frac{1}{3}\mathbf{W}^{(*),\mathbf{G}}_{i+\frac{1}{2},j+3}\right)\\&+\omega^{(1)}\left(\frac{1}{3}\mathbf{W}^{(*),\mathbf{G}}_{i+\frac{1}{2},j}+\frac{5}{6}\mathbf{W}^{(*),\mathbf{G}}_{i+\frac{1}{2},j+1}-\frac{1}{6}\mathbf{W}^{(*),\mathbf{G}}_{i+\frac{1}{2},j+2}\right)\\&+\omega^{(2)}\left(-\frac{1}{6}\mathbf{W}^{(*),\mathbf{G}}_{i+\frac{1}{2},j-1}+\frac{5}{6}\mathbf{W}^{(*),\mathbf{G}}_{i+\frac{1}{2},j}+\frac{1}{3}\mathbf{W}^{(*),\mathbf{G}}_{i+\frac{1}{2},j+1}\right).\end{aligned} \tag{4.23}$$

Here, $(*U)=(LU),(RU)$. Eventually, conservative variables at corner C_1 are obtained as

$$\mathbf{U}^{*}_{i+\frac{1}{2},j+\frac{1}{2}}=\mathbf{R}^{\mathbf{G}}_{i+\frac{1}{2},j+\frac{1}{2}}\mathbf{W}^{(*),\mathbf{G}}_{i+\frac{1}{2},j+\frac{1}{2}}, \tag{4.24}$$

where $*=LD,LU,RD,RU$.

It should be noted that the reconstruction of conservative variables at different corners is independent of each other, and the reconstruction procedure of Eqs. (4.18) to (4.23) should be repeated at each corner. In addition, as shown in Eq. (4.18), an identical left characteristic matrix is used to calculate characteristic variables in 36 cells around the corner to form the stencils. In fact, in the dimension-by-dimension reconstruction procedure, the characteristic matrices in Eqs. (4.18), (4.21) and (4.24) are always defined at corner $(i+\frac{1}{2},j+\frac{1}{2})$, and they are evaluated through $\mathbf{U}_{i+\frac{1}{2},j+\frac{1}{2}}$. Here, $\mathbf{U}_{i+\frac{1}{2},j+\frac{1}{2}}$ is defined as

$$\mathbf{U}_{i+\frac{1}{2},j+\frac{1}{2}}=\left(\mathbf{U}_{i,j+1}+\mathbf{U}_{i,j}+\mathbf{U}_{i+1,j}+\mathbf{U}_{i+1,j+1}\right)/4.$$

As shown in Eq. (4.18), although the repeated calculation of characteristic variables required for reconstruction of variables at different corners is slightly expensive, it might be necessary in order to avoid spurious oscillations. Therefore, the algorithm described in Eqs. (4.18) to (4.24) is adopted to obtain conservative variables at corners in numerical tests in Section 5.

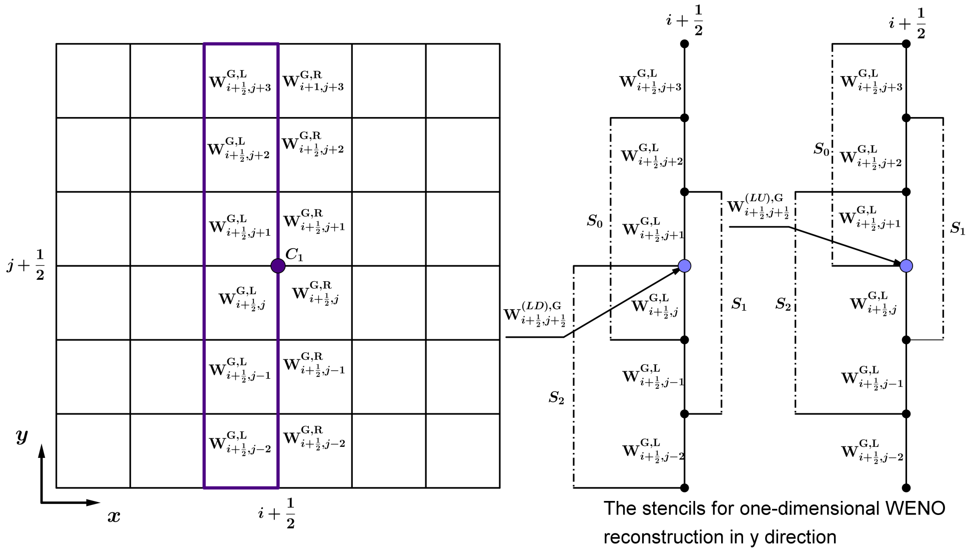

Figure 3: Illustration of the stencils of one-dimensional WENO reconstruction in y direction to approximate characteristic variables at corner $(i+\frac{1}{2},j+\frac{1}{2})$.

5 Numerical results

The update steps of conservative variables

1) Calculate the values of characteristic variables at the midpoints of interfaces through Eqs. (4.6), (4.10), (4.15) and (4.16), respectively. Obtain the values of conserved variable vectors at the midpoints of interfaces using Eq. (4.11).

2) Calculate fluxes at midpoints of interfaces using Eq. (3.2) and (3.5).

3) Evaluate the states of characteristic variables at corners using Eq. (4.22) and (4.23), respectively. Then, calculate the values of the conserved variable vectors at corners through Eq. (4.24).

4) Evaluate fluxes at corners using Eqs. (3.7), (3.8), (3.9a) and (3.9b).

5) Obtain the total flux through an interface using Eq. (3.12).

6) Substitute total flux through an interface into Eq. (2.4) and update conserved variable vectors according to Eq. (2.5).

A series of 1D and 2D test problems are calculate to validate the performance of the genuinely multidimensional HLL-CPS solver (GM-HLL-CPS) based on the fifth-order WENO reconstruction method.

5.1 1D Riemann problem

Three one-dimensional Riemann problems are calculated to show the performance of the proposed scheme. The parameter settings of the three problems are presented in Table 1, in which x_0 is the location of discontinuity and T is the computing time. The numerical results calculated by the GM-HLL-CPS scheme are compared with the results obtained from the one-dimensional HLL-CPS scheme. The fifth-order WENO reconstruction method is used to approximate the values of conservative variables. In addition, we also show the solutions of the GM-HLL-CPS scheme based on the SDWLS method. The domain $[0,1]$ is uniformly divided into 200 cells.

The results in Fig. 4 show that two types of fifth-order schemes have higher resolution for contact discontinuity and shock wave than the second-order scheme. In ad-

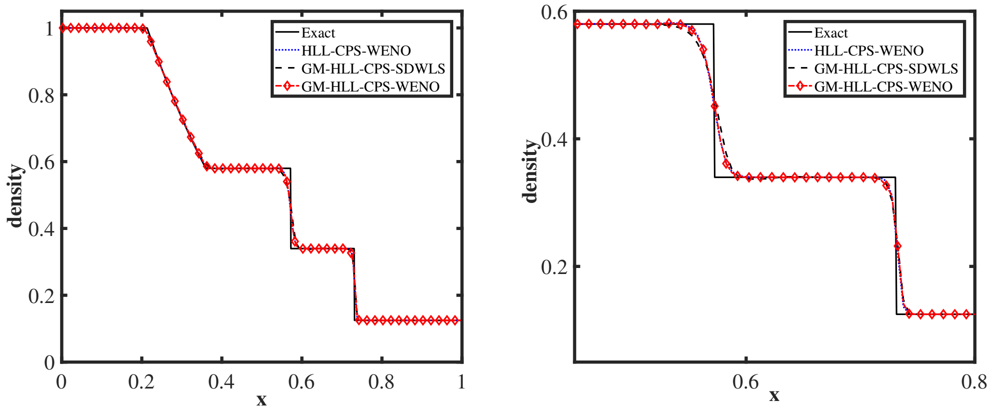

(a) Solution of case1 (b) Local amplification of case1

Figure 4: Numerical results of case1.

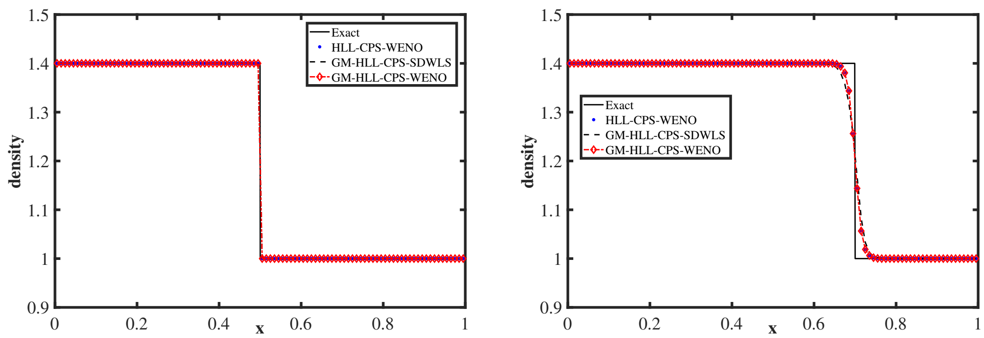

(a) Solution of case2 (b) Solution of case3

Figure 5: Numerical results of case2 and case3.

Table 1: The initial parameters of three 1D Riemann problems.

Cases	$(\rho,u,p)_L$	$(\rho,u,p)_R$	x_0	T
Case1	(1.0,0.75,1.0)	(0.125,0.0,0.1)	0.3	0.2
Case2	(1.4,0.0,1.0)	(1.0,0.0,1.0)	0.5	2
Case3	(1.4,0.1,1.0)	(1.0,0.1,1.0)	0.5	2

dition, due to no flow feature propagating along the transverse direction in the purely one-dimensional problems, the numerical results calculated by the one-dimensional and two-dimensional HLL-CPS solvers with fifth-order reconstruction are similar. The solutions of case2 and case3 are plotted in Fig. 5, from which it can be clearly observed that the fifth-order schemes provide higher resolution than the second-order scheme.

The numerical results of three one-dimensional test problems demonstrate two types of fifth-order schemes have higher accuracy than the second-order scheme and in the simulations of one-dimensional problems, the 1D solver and the genuinely 2D solver with the same reconstruction method have similar performances, which is in good agreement with the expectation. All of these indicate that the reconstruction methods carried out in the present work are reasonable.

5.2 2D Riemann problems

Three two-dimensional Riemann problems are simulated in this section and we adopt the notation used in [49] to name these problems.

Firstly, a two-dimensional Riemann problem described by Brio et al. [19] is solved to examine the resolution of the present method. Its initial conditions are given as

$$(\rho,\, u,\, v,\, p)=\begin{cases}(1.0,\, 0.7276,\, 0.0,\, 1.0), & \text{if } x<0.0, \quad y>0.0,\\ (0.5313,\, 0.0,\, 0.0,\, 0.4), & \text{if } x>0.0, \quad y>0.0,\\ (1.0,\, 0.0,\, 0.7276,\, 1.0), & \text{if } x>0.0, \quad y<0.0,\\ (0.8,\, 0.0,\, 0.0,\, 1.0), & \text{if } x<0.0, \quad y<0.0.\end{cases}$$

The initial state consists of two contact discontinuities and two forward shock waves, namely, $\vec{S}_{21}J_{32}J_{34}\vec{S}_{41}$. The computational domain $[-1,1]\times[-1,1]$ is divided into 400×400 uniform cells. The density contours obtained from three one-dimensional solvers with $\mathrm{CFL}=0.4$ and GM-HLL-CPS solver with $\mathrm{CFL}=0.8$ at $t=0.5$ are plotted in Fig. 6. The numerical solution consists of two Mach reflection stems and two contact waves at the intersection of the four shock waves [3]. It can be obviously observed that there is no non-physical oscillation in the solutions obtained from these four solvers. Compared with the HLLE solver, other three solvers produce solutions with higher resolution due to their desirable ability of capturing contact waves. The higher order accuracy from the WENO method makes the advantage of the GM-HLL-CPS solver to be unconspicuous for this test case. But the GM-HLL-CPS solver permits a larger CFL number up to 0.8, while the CFL number for one-dimensional solvers should be less than 0.5.

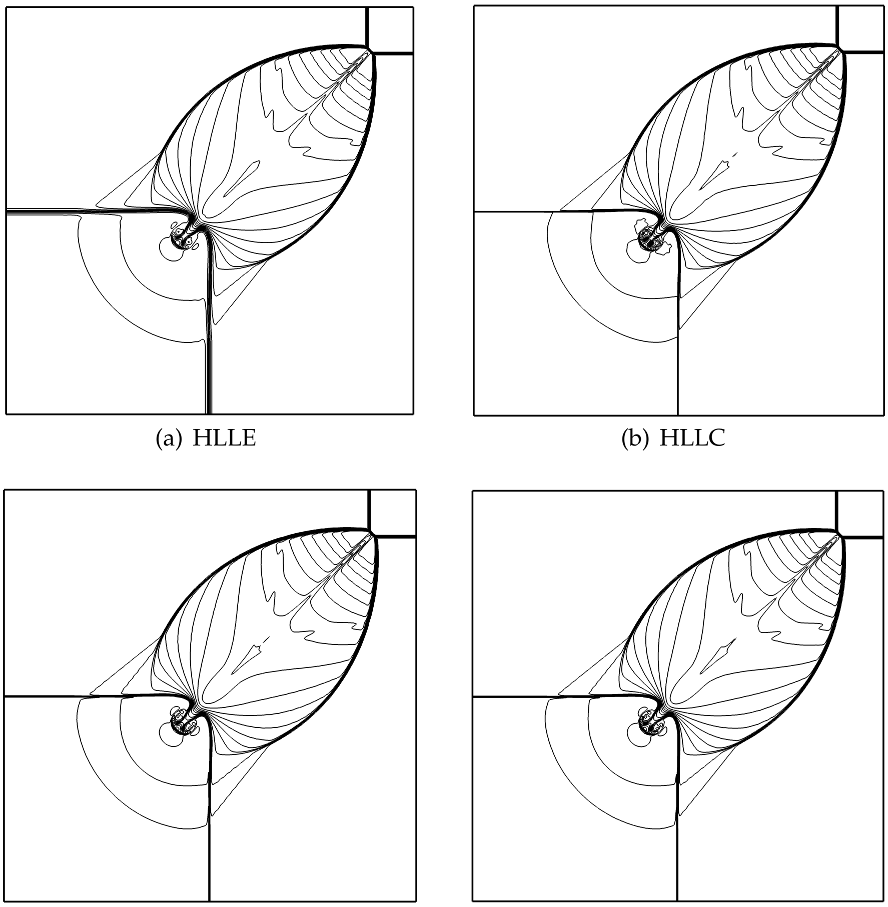

(a) HLLE (b) HLLC (c) HLL-CPS (d) GM-HLL-CPS

Figure 6: Density contours of the first 2D Riemann problem at $t=0.5$.

The initial conditions of the second 2D Riemann problem are given by

$$(\rho,\, u,\, v,\, p)=\begin{cases}(2.0,0.75,0.5,1.0), & \text{if } x<0.5, \quad y>0.5,\\ (1.0,0.75,-0.5,0.4), & \text{if } x>0.5, \quad y>0.5,\\ (3.0,-0.75,-0.5,1.0), & \text{if } x>0.5, \quad y<0.5,\\ (1.0,-0.75,0.5,1.0), & \text{if } x<0.5, \quad y<0.5.\end{cases}$$

It can be named as $\vec{J}_{21}\vec{J}_{32}\vec{J}_{34}\vec{J}_{41}$. The wave configurations are composed of four moving contact waves. Although the mathematical model of this problem is inviscid, the numerical viscosity introduced by numerical schemes is capable of triggering the shear instability [32]. Therefore, the numerical results of this case can reveal the capacity of schemes to resolve the contact discontinuities and shear layers. The computation is run

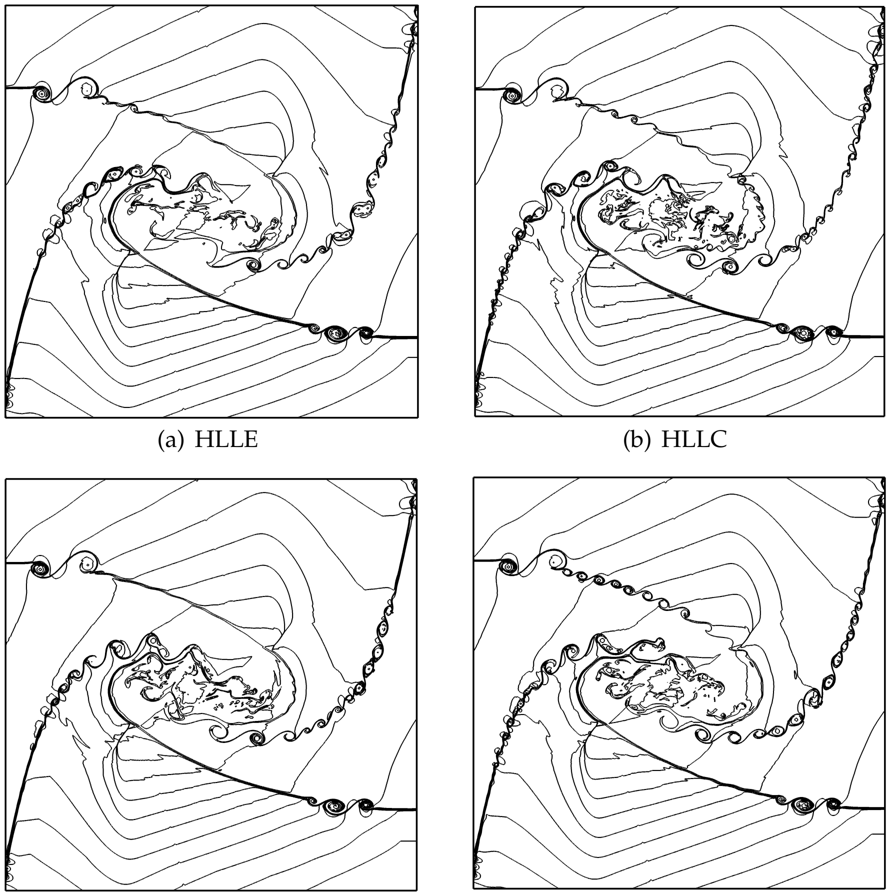

(a) HLLE (b) HLLC

(c) HLL-CPS (d) GM-HLL-CPS

Figure 7: Density contours of the second 2D Riemann problem at $t=0.7$.

on a 1600×1600 uniform mesh which covers a domain of $[0,1]\times[0,1]$ and it ends till time $t=0.7$. The density contours at the final time are shown in Fig. 7. Due to the high accuracy of the WENO scheme, it can be clearly observed that all of four solvers resolve the shear layers accurately and capture the complex vortex-type structures caused by the Kelvin-Helmholtz instability [32]. However, compared with the three 1D solvers, the GM-HLL-CPS scheme produces the solution with more details. Numerical results indicate that the GM-HLL-CPS scheme improves the ability to resolve accurate solution for 2D problems owing to considering the flow information traveling along the transverse direction.

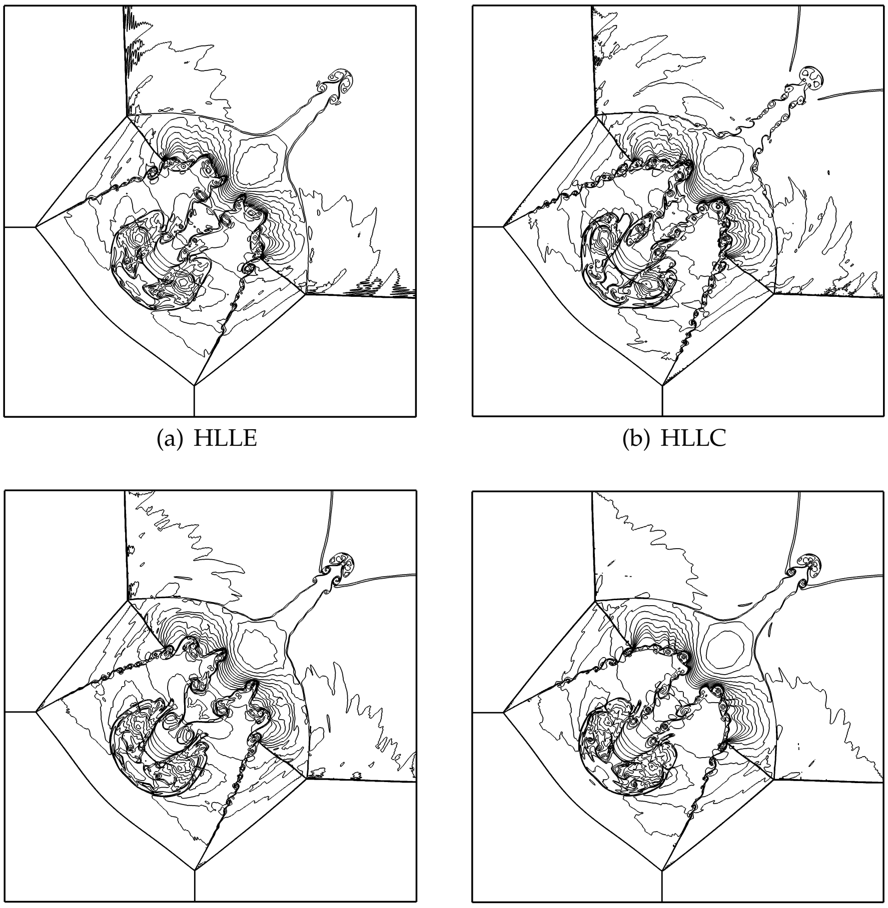

(a) HLLE (b) HLLC

(c) HLL-CPS (d) GM-HLL-CPS

Figure 8: Density contours of the third 2D Riemann problem at $t=0.8$.

The initial conditions of the third 2D Riemann problem are set as

$$(\rho, u, v, p)=\begin{cases} (0.5323,1.206,0.0,0.3), & \text{if } x<0.8, \quad y>0.8, \\ (1.5,0.0,0.0,1.5), & \text{if } x>0.8, \quad y>0.8, \\ (0.5323,0.0,1.206,0.3), & \text{if } x>0.8, \quad y<0.8, \\ (0.138,1.206,1.206,0.029), & \text{if } x<0.8, \quad y<0.8. \end{cases}$$

During its evolution, the initial configuration results in a double Mach reflection and a shock propagating at a 45° angle to the grid lines. The numerical simulation is run on a computational domain $[0,1]\times[0,1]$ covered by a 800×800 uniform Cartesian mesh. The density distributions obtained from the HLLE, HLLC, HLL-CPS and GM-HLL-CPS solvers at $t=0.8$ are shown in Fig. 8. With the help of the fifth-order WENO reconstruction, four solvers accurately resolve the vortical structures at the Mach stem. However, the solution resolved by the HLLC solver is not symmetric. In addition, although both of the HLLE and HLL-CPS schemes obtain symmetry solutions, the greater details in the Mach stem resolved by GM-HLL-CPS solver still imply that the multidimensionality greatly improves the resolution of the scheme. Meanwhile, the GM-HLL-CPS scheme can select a larger CFL number. Specifically, in this test, the CFL number can set to 0.85 for the GM-HLL-CPS solver while it can not exceed 0.5 for one-dimensional solvers.

5.3 Radial Riemann problem

Here, we consider a radial Riemann problem. At the initial moment, the stationary high-pressure gas is located in a circular region in the center of domain $[0,1]\times[0,1]$, and the rest of the domain is filled with stationary, low-pressure gas. The initial states in the whole domain are set as

$$(\rho,\ u,\ v,\ p)=\begin{cases} (2,\ 0,\ 0,\ 15), & \text{if } r<0.13, \\ (1,\ 0,\ 0,\ 2), & \text{otherwise,} \end{cases}$$

where r is the radius. The problem is run on a uniform mesh with 200×200 cells. The density contours of this problem resolved by three one-dimensional solvers with a CFL number of 0.45 and the GM-HLL-CPS solver with a CFL number of 0.85 at $t=0.13$ are plotted in Fig. 9. It can be observed that there is no obvious non-physical oscillation in the solutions and the outward shock fronts are very sharp and clear. The CFL number is usually limited to 0.5 for 1D solvers while it can be up to 0.85 for the GM-HLL-CPS solver. This test case verify again that the multidimensionality of the genuinely multi-dimensional solver permits a larger CFL number in simulations of 2D flow problems.

5.4 Random numerical noises problem

In the computational domain $[0,300]\times[0,30]$, a Mach 10 plane right-moving shock initially located at $x=5$ propagates along the x-direction. A uniform Cartesian mesh with 300×30 cells is used to cover the domain. The upstream condition is chosen to be $(\rho,u,v,p)=(1.4,0,0,1)$ on the left boundary while the downstream condition obtained through the exact shock relations is used on the right boundary. The reflective condition is used at the top and bottom boundaries. In order to trigger the multidimensionality, random perturbations ranging from -10^{-5} to 10^{-5} are initially introduced into the upstream region as follows

$$(\rho,u,v,p)_{i,j}=(1.4,0,0,1)+(\alpha_1,\alpha_2,\alpha_3,\alpha_4)_{i,j}\cdot 10^{-5},\quad x>5,$$

where α_k $(k=1,2,3,4)$ are random numbers between -1.0 and 1.0. The CFL number for 1D solvers are set to 0.3 while the CFL number of the GM-HLL-CPS solver is chosen as 0.85. Fig. 10 plots the density contours at $t=20$, from which it is clearly observed that

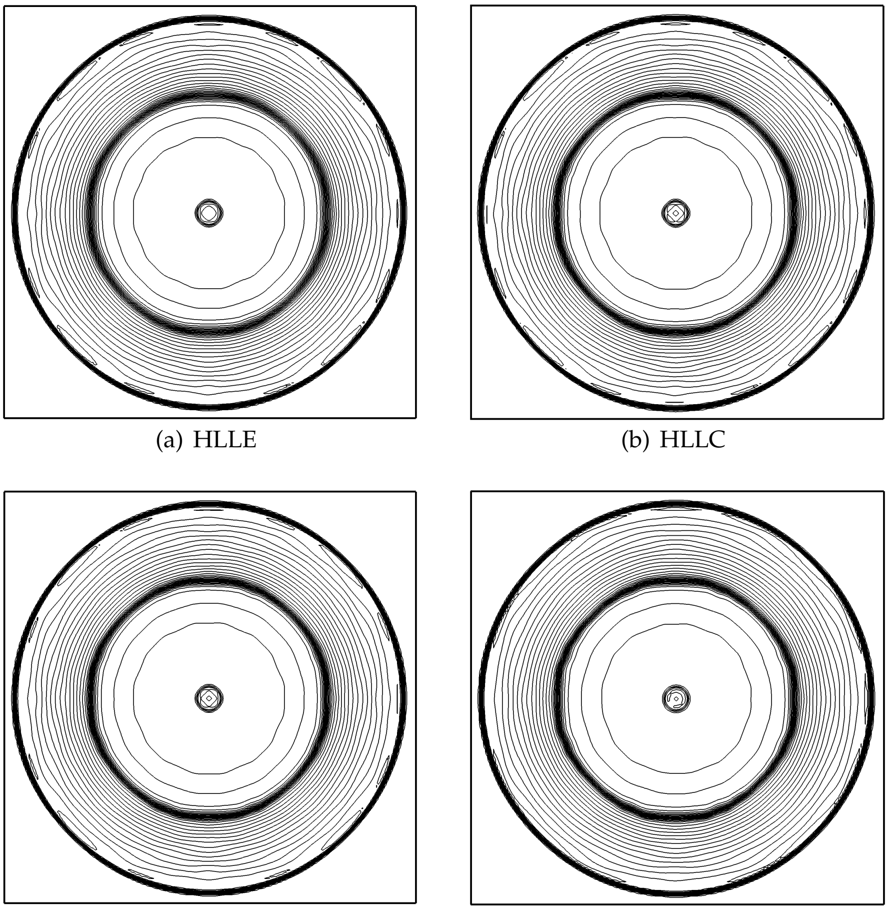

(a) HLLE (b) HLLC

(c) HLL-CPS (d) GM-HLL-CPS

Figure 9: Results of the radial Riemann problem at $t=0.13$.

the solution obtained from the HLLC scheme displays severe instabilities, while other schemes eliminate the shock anomalies and exhibit the clear shock fronts.

5.5 Double Mach reflection problem

In the domain $[0,4]\times[0,1]$, a Mach 10 oblique shock, making a 60 angle with the bottom wall, interacts with the bottom wall at $x=1/6$. The initial configurations are set as

$$(\rho,\, u,\, v,\, p)=\begin{cases} (1.4,0,0,1), & \text{if } y<\sqrt{3}\Big(x-\dfrac{1}{6}\Big), \\ \Big(8,\dfrac{33\sqrt{3}}{8},-4.125,116.5\Big), & \text{else.} \end{cases}$$

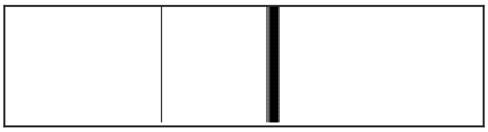

(a) HLLE

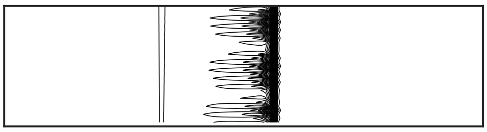

(b) HLLC

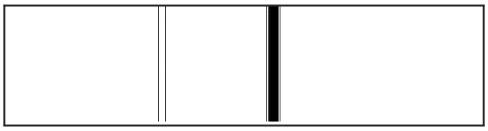

(c) HLL-CPS

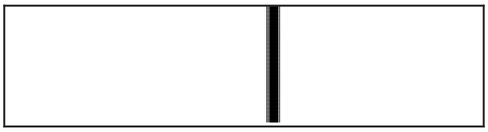

(d) GM-HLL-CPS

Figure 10: Density contours of the random numerical noises problem at $t=20$.

(a) HLLE

(b) HLLC

(c) HLL-CPS

(d) GM-HLL-CPS

Figure 11: Results of the double Mach reflection problem at $t=0.2$.

The downstream condition is imposed at the left boundary while the values of the ghost cells at the right boundaries are directly extrapolated from the adjacent interior cells with zero gradient. For the bottom boundary, downstream conditions are used from $x=0$ to $x=1/6$ while reflective conditions are adopted for the rest cells. The boundary conditions at the top are adjusted to follow the motion of the shock. The simulation is implemented on a 960×480 Cartesian mesh and ended at $t=0.2$. The density profiles at the final time are displayed in Fig. 11. It is clear observed that the solutions calculated by the HLLE, HLL-CPS and GM-HLL-CPS solvers are free from any non-physical oscillation, while the HLLC solver produces a relatively unstable solution due to its low dissipation property.

5.6 Forward facing step problem

In the domain $[0,3]\times[0,1]$, a Mach 3 flow travels through a channel including a step with the corner locating at $(x,y)=(0.6,0.2)$. A uniform Cartesian mesh with 480×160 cells is employed to cover the domain. The initial values of entire domain is set to $(\rho_0,u_0,v_0,p_0)=(1.4,3.0,0.0,1.0)$. The inflow conditions are imposed at the left boundary while the values of the ghost cells at the right boundary are directly extrapolated from the adjacent interior cells with zero gradient. At the inviscid walls of the top and bottom boundaries, the reflective conditions are used. Fig. 12 shows the density profiles. It is clearly observed that three 1D solvers give solutions with severe kinked stems in the reflective waves while the GM-HLL-CPS solver produces a shock profile without visible instabilities and eliminates the notorious kink.

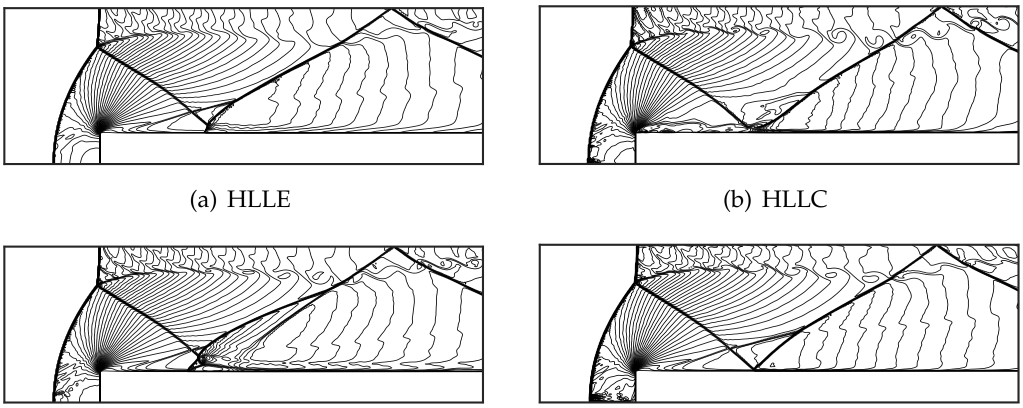

(a) HLLE (b) HLLC

(c) HLL-CPS (d) GM-HLL-CPS

Figure 12: Results of the forward facing step problem at $t=4$.

5.7 Richtmeyer-Meshkov instability problem

In the domain of $[0,4]\times[0,1]$, a perturbed interface is initially located at

$$x_p=2.9-0.1\sin(2\pi(y+0.25)).$$

Two fluids with different densities are separated by the perturbed interface. On the right of the perturbed interface, a left-moving shock is placed. The initial conditions are given

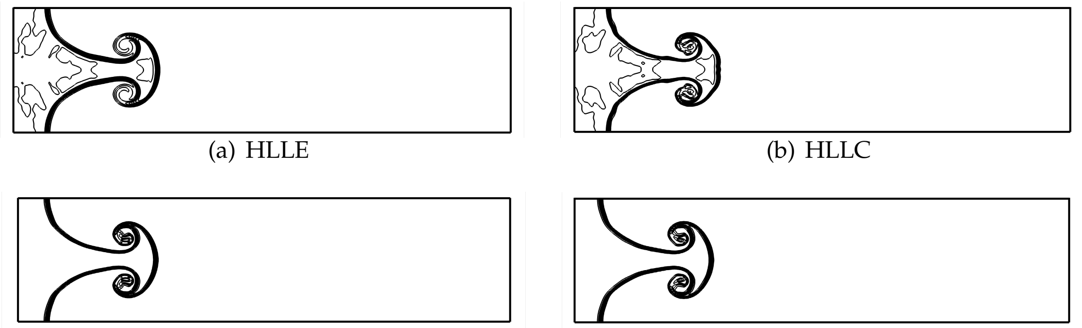

(a) HLLE (b) HLLC

(c) HLL-CPS (d) GM-HLL-CPS

Figure 13: Results of the Richtmeyer-Meshkov instability problem at $t=9$.

as

$$(\rho,\, u,\, v,\, p)=\begin{cases} (5.04,0,0,1), & \text{if } 0\le x<x_p, \\ (1,0,0,1), & \text{if } x_p\le x<3.2, \\ (1.4112,-665/1556,0,1.628), & \text{if } 3.2\le x. \end{cases}$$

The periodic boundary conditions are employed at the bottom and top boundaries and the non-reflective conditions are used at the left and right boundaries. The 640×160 uniform mesh is used to cover the domain and the computation is ended at $t=9$. The density contours calculated by four solvers are plotted in Fig. 13. It is evident that the HLLE and HLLC solvers produce solutions with visible numerical oscillation at the left side of the density interface while the density interfaces obtained from the HLL-CPS and GM-HLL-CPS solvers are smooth enough.

5.8 Rayleigh-Taylor instability problem

In order to investigate the inherent numerical dissipation of the proposed scheme, the famous Rayleigh-Taylor instability problem is considered here. The specific heat ratio $\gamma=5/3$ in this test case. The initial states are given as

$$(\rho,\, u,\, v,\, p)=\begin{cases} (2,0,-0.025a_0\cos(8\pi x),1+2y), & \text{if } 0\le y<0.5, \\ (1,0,-0.025a_0\cos(8\pi x),1.5+y), & \text{if } 0.5<\, y\le1.0, \end{cases}$$

where $a_0=\sqrt{\gamma p_0/\rho_0}$ is the initial speed of sound. The state at the top boundary is assigned as $(\rho,u,v,p)=(1,0,0,2.5)$ and the state on the bottom boundary is set to $(\rho,u,v,p)=(2,0,0,1)$. Under the drive of the gravity effect, the heavier fluid falls into the lighter one and the bubble rises to the heavier fluid. Reflective conditions are employed for the left and right boundaries. This test case is run on a 256×1024 uniform Cartesian mesh. Fig. 14 shows the density contours at $t=1.95$. Numerical results clearly

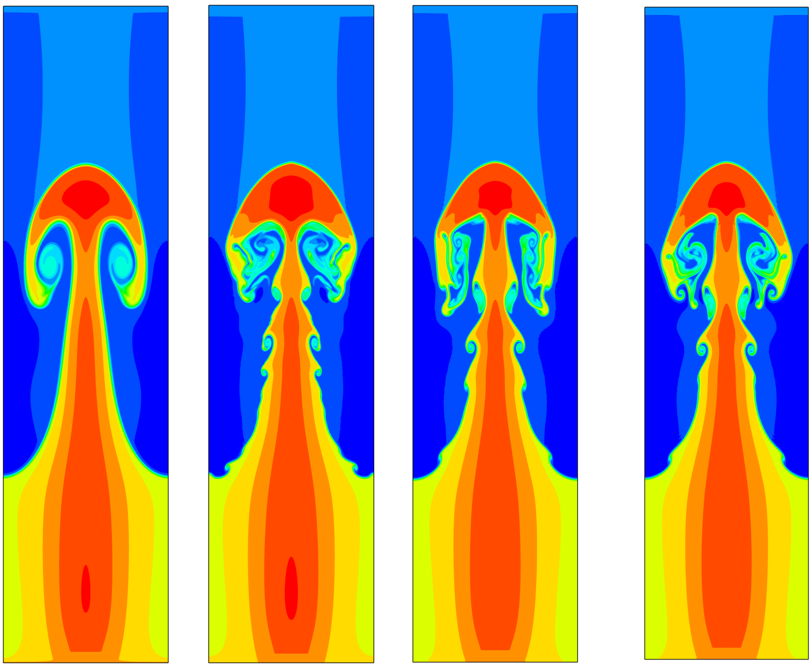

(a) HLLE (b)HLLC (c) HLL-CPS (d) GM-HLL-CPS

Figure 14: Density contours of the Rayleigh-Taylor instability problem at $t=1.95$.

indicate that the GM-HLL-CPS solver is able to resolve small scale structures with higher resolution.

5.9 Kelvin-Helmholtz instability problem

In a square domain $[-0.5,0.5]\times[-0.5,0.5]$ which is covered by a 640×640 uniform mesh, fluids with different densities are separated by two interfaces located at $y=-0.25$ and $y=0.25$. The initial linear perturbation of the velocity in the y direction triggers vortexes emerging at the sharp density interfaces owing to the Kelvin-Helmholtz instability [47]. The growth of vortexes and the interaction between them will form a turbulence regime [46]. The initial states are given as

$$(\rho,u,v,p)=\begin{cases}(1,0.5,0.01\sin(2\pi x),2.5), & \text{if } y<-0.25,\\ (2,-0.5,0.01\sin(2\pi x),2.5), & \text{if } -0.25<y<0.25,\\ (1,0.5,0.01\sin(2\pi x),2.5), & \text{if } 0.25<y.\end{cases}$$

Periodic boundary conditions are employed at all boundaries. Fig. 15 plots the density contours obtained from four solvers at time $t=2$. It can be clearly observed that the

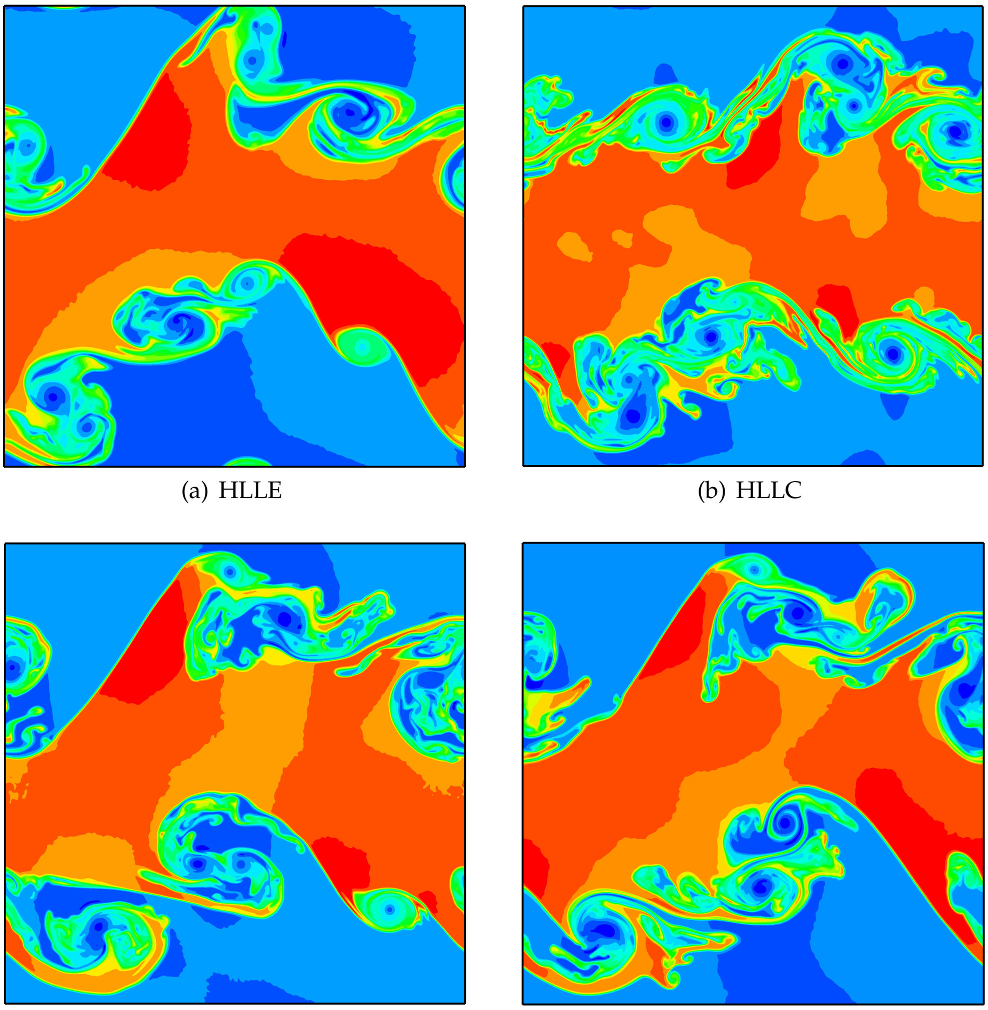

(a) HLLE (b) HLLC

(c) HLL-CPS (d) GM-HLL-CPS

Figure 15: Density contours of the Kelvin-Helmholtz instability problem.

HLLC scheme produces the most accurate result with complex vortex structures. Comparing with the 1D HLL-CPS solver, the GM-HLL-CPS solver obtains a relatively accurate solution with more vortexes structures nearby the density interfaces.

6 Conclusions

In this work, a high-order reconstruction method is presented for the genuinely multi-dimensional HLL-CPS Riemann solver. The conservative vectors at midpoints of interfaces are reconstructed by the fifth-order WENO reconstruction. Meanwhile, variables at corners are evaluated by a dimension-by-dimension reconstruction method consisting of a number of one-dimensional fifth-order WENO reconstruction sweeps in the x and y-directions. To ensure numerical stability, each reconstruction step is carried out in the corresponding characteristic field. A series of benchmark numerical experiments are conducted to demonstrate the performance of the proposed scheme in accuracy, resolution and robustness. Numerical results of the 1D test cases give fully proof that, with the help of the proposed reconstruction method, the present genuinely multidimensional HLL-CPS solver is more accurate than its low-order version. It is demonstrated by the 2D Riemann problems that the multidimensionality property of the high-order GM-HLL-CPS scheme brings higher accuracy and resolution in resolving sharp contact discontinuities over the HLLE, HLLC and the 1D HLL-CPS schemes. And more importantly, the proposed high-order genuinely multidimensional HLL-CPS solver presents better robustness against the shock anomalies.

Acknowledgements

This work was supported by National Natural Science Foundation of China (Nos. 12271464), Hunan Provincial Natural Science Foundation of China (Nos. 2023JJ10038, 2021JJ40009, 2021JJ10038, 2021JJ30056), Excellent Youth Project of Hunan Education Department, China (Nos. 21B0626, 20B574). In addition, we would like to thank Prof. Xiayi Hu for his enthusiastic encouragement and patient guidance during this study.

References

[1] F. ARÀNDIGA, A. BAEZA, A. BAEZA AND P. MULET, *Analysis of WENO schemes for full and global accuracy,* SIAM J. Numer. Anal., 49(2) (2011), pp. 893–915.

[2] D. BALSARA, *Multidimensional HLLE Riemann solver: Application to Euler and magnetohydrodynamic flows,* J. Computat. Phys., 229(6) (2010), pp. 1970–1993.

[3] D. BALSARA, *A two-dimensional HLLC Riemann solver for conservation laws: Application to Euler and magnetohydrodynamic flows,* J. Computat. Phys., 231(22) (2012), pp. 7476–7503.

[4] D. BALSARA, *Three dimensional HLL Riemann solver for conservation laws on structured meshes; Application to Euler and magnetohydrodynamic flows,* J. Computat. Phys., 295 (2015), pp. 1–23.

[5] D. BALSARA AND M. DUMBSER, *Divergence-free MHD on unstructured meshes using high order finite volume schemes based on multidimensional Riemann solvers,* J. Computat. Phys., 299 (2015), pp. 687–715.

[6] D. BALSARA, S. SAMANTARAY AND S. SUBRAMANIAN, *Efficient WENO-based prolongation strategies for divergence-preserving vector fields,* Commun. Appl. Math. Comput., 5(05) (2022), pp. 428–484.

[7] D. BALSARA AND M. DUMBSER, *Multidimensional Riemann problem with self-similar internal structure. Part II–Application to hyperbolic conservation laws on unstructured meshes,* J. Computat. Phys., 287 (2015), pp. 269–292.

[8] D. Balsara, M. Dumbser and R. Abgrall, *Multidimensional HLLC Riemann solver for unstructured meshes–With application to Euler and MHD flows,* J. Computat. Phys., 261 (2014), pp. 172–208.
[9] D. Balsara, S. Garain, V. Florinski and W. Boscheri, *An efficient class of WENO schemes with adaptive order for unstructured meshes,* J. Computat. Phys., 404 (2020), 109062.
[10] D. Balsara, S, Garain and C.-W. Shu, *An efficient class of WENO schemes with adaptive order,* J. Computat. Phys., 326 (2016), pp. 780–804.
[11] D. Balsara and J. Kim, *A subluminal relativistic magnetohydrodynamics scheme with ADER-WENO predictor and multidimensional Riemann solver-based corrector,* J. Computat. Phys., 312 (2016), pp. 357–384.
[12] D. Balsara and B. Nkonga, *Multidimensional Riemann problem with self-similar internal structure–part III–a multidimensional analogue of the HLLI Riemann solver for conservative hyperbolic systems,* J. Computat. Phys., 346 (2017), pp. 25–48.
[13] D. Balsara and C.-W. Shu, *Monotonicity preserving weighted essentially non-oscillatory schemes with increasingly high order of accuracy,* J. Computat. Phys., 160(2) (2000), pp. 405–452.
[14] D. Balsara, A. Taflove, S. Garain and Gino Montecinos, *Computational electrodynamics in material media with constraint-preservation, multidimensional Riemann solvers and sub-cell resolution–Part I, second-order FVTD schemes,* J. Computat. Phys., 349 (2017), pp. 604–635.
[15] D. Balsara, J. Vides, K. Gurski, B. Nkonga, M. Dumbser, S. Garain and E. Audit, *A two-dimensional Riemann solver with self-similar sub-structure-Alternative formulation based on least squares projection,* J. Computat. Phys., 304 (2016), pp. 138–161.
[16] S. J. Billett and E. F. Toro, *On WAF-type schemes for multidimensional hyperbolic conservation laws,* J. Computat. Phys., 130(1) (1997), pp. 1–24.
[17] K. Borah, G. Natarajan and A. Dass, *A novel second-order flux splitting for ideal magnetohydrodynamics,* J. Computat. Phys., 313(05) (2016), pp. 159–180.
[18] W. Boscheri, D. Balsara and M. Dumbser, *Lagrangian ADER-WENO finite volume schemes on unstructured triangular meshes based on genuinely multidimensional HLL Riemann solvers,* J. Computat. Phys., 267 (2014), pp. 112–138.
[19] M. Brio, A. R. Zakharian and G. M. Webb, *Two-dimensional Riemann solver for Euler equations of gas dynamics,* J. Computat. Phys., 167 (1) (2001), pp. 177–195.
[20] P. Colella, *Multidimensional upwind methods for hyperbolic conservation laws,* J. Computat. Phys., 87 (1990), pp. 171–200.
[21] V. Coralic and T. Colonius, *Finite-volume WENO scheme for viscous compressible multicomponent flows,* J. Computat. Phys., 274 (2014), pp. 95–121.
[22] M. Dumbser and D. Balsara, *A new efficient formuslation of the HLLEM Riemann solver for general conservative and non-conservative hyperbolic systems,* J. Computat. Phys., 304 (2016), pp. 275–319.
[23] B. Engquist and S. Osher, *One-sided difference approximations for nonlinear conservation laws,* J. Computat. Phys., 36(154) (1981), pp. 321–351.
[24] M. Fey, *Multidimensional upwinding. part i. the method of transport for solving the Euler equations,* J. Computat. Phys., 143(1) (1998), pp. 159–180.
[25] G. Gerolymos, D. Sénéchal, and I. Vallet, *Very-high-order WENO schemes,* J. Computat. Phys., 228(23) (2009), pp. 8481–8524.
[26] S. Gudonov, *The finite-difference method for the computation of discontinuous solutions of the equations of fluid dynamics,* J. Computat. Phys., 47(01) (1959), pp. 357–393.
[27] Y. Guo, W. Yang, H. Zhang, J. Wang and S. Song, *A splitting method for the Degasperis-*

Procesi equation using an optimized WENO scheme and the Fourier pseudospectral method, Adv. Appl. Math. Mech., 11 (2019), pp. 53–71.

[28] A. HARTEN, B. ENGQUIST, S. OSHER AND S. CHAKRAVARTHY, *Uniformly high order accurate essentially non-oscillatory schemes, III,* J. Computat. Phys., 71(2) (1987), pp. 231–303.

[29] A. HARTEN, P. D. LAX AND B. VAN LEER, *On upstream differencing and Godunov-type schemes for hyperbolic conservation laws,* SIAM Rev., 25(1) (1983), pp. 35–61.

[30] L. HU AND S. FENG, An accurate and shock-stable genuinely multidimensional scheme for solving the Euler equations, Commun. Nonlinear Sci. Numer. Simul., 97(1) (2021), 105738.

[31] L. HU AND L. YUAN, *A genuinely multidimensional Riemann solver based on the TV splitting,* Appl. Math. Mech., 38 (2017), pp. 243–264.

[32] L. HU AND L. YUAN, *A simple FORCE-type centred scheme accurate for contact discontinuities: Application to compressible Euler flows,* Comput. Fluids, 227 (2021), 105021.

[33] L. HU, L. YUAN AND K. ZHAO, *Development of accurate and robust genuinely two-dimensional HLL-type Riemann solver for compressible flows,* Comput. Fluids, 213 (2020), 104719.

[34] G. S. JIANG AND C.-W. SHU, *Efficient implementation of weighted ENO schemes,* J. Computat. Phys., 126(1) (1996), pp. 202–228.

[35] K. H. KIM, C. KIM AND O. H. RHO, *Methods for the accurate computations of hypersonic flows: I. AUSMPW+ scheme,* J. Computat. Phys., 174(1) (2001), pp. 38–80.

[36] R. J. LEVEQUE, *Wave propagation algorithms for multidimensional hyperbolic systems,* J. Computat. Phys., 131(2) (1997), pp. 327–353.

[37] M.-S. LIOU AND C. J. STEFFEN, *A new flux splitting scheme,* J. Computat. Phys., 107(1) (1993), pp. 23–39.

[38] X.-D. LIU, S. OSHER AND T. CHAN, *Weighted essentially non-oscillatory schemes,* J. Computat. Phys., 115(1) (1994), pp. 200–212.

[39] J. C. MANDAL AND V. PANWAR, *Robust HLL-type Riemann solver capable of resolving contact discontinuity,* Comput. Fluids, 63(1) (2012), pp. 148–164.

[40] J. C. MANDAL AND V. SHARMA, *A genuinely multidimensional convective pressure flux split Riemann solver for Euler equations,* J. Computat. Phys., 297 (2015), pp. 669–688.

[41] F. QU, D. SUN AND C. YAN, *A new flux splitting scheme for the Euler equations II: E-AUSMPWAS for all speeds,* Commun. Nonlinear Sci. Numer. Simul., 57 (2018), pp. 58–79.

[42] F. QU, D. SUN, B. ZHOU AND J. BAI, *Self-similar structures based genuinely two-dimensional Riemann solvers in curvilinear coordinates,* J. Computat. Phys., 420 (2020), 109668.

[43] UTTAM SINGH RAJPUT AND KRISHNA MOHAN SINGH, *A fifth order alternative mapped WENO scheme for nonlinear hyperbolic conservation laws,* Adv. Appl. Math. Mech., 14 (2022), pp. 275–298.

[44] P. ROE, *Approximate Riemann solvers, parameter vector, and difference schemes,* J. Computat. Phys., 43(10) (1981), pp. 357–372.

[45] C. RUMSEY, B. VAN LEER AND P. ROE, *A multidimensional flux function with applications to the Euler and Navier-Stokes equations,* J. Computat. Phys., 105(2) (1993), pp. 306–323.

[46] O. SAN AND K. KARA, *Evaluation of Riemann flux solvers for WENO reconstruction schemes: Kelvin–Helmholtz instability,* Comput. Fluids, 117 (2015), pp. 24–41.

[47] O. SAN AND A. STAPLES, *High-order methods for decaying two-dimensional homogeneous isotropic turbulence,* Comput. Fluids, 63 (2012), pp. 105–127.

[48] K. SCHNEIDER, J. GALLARDO, D. BALSARA, B. NKONGA AND C. PARÉS, *Multidimensional approximate Riemann solvers for hyperbolic nonconservative systems. Applications to shallow water systems,* J. Computat. Phys., 444 (2021), 110547.

[49] C. SCHULZ-RINNE, J. COLLINS AND H. GLAZ, *Numerical solution of the Riemann problem for*

two-dimensional gas dynamics, SIAM J. Sci. Comput., 14(6) (1993), pp. 1394–1414.

[50] C.-W. SHU, *Total-variation-diminishing time discretizations,* SIAM J. Sci. Stat. Comput., 9(6) (1988), pp. 1073–1084.

[51] C.-W. SHU, B. COCKBURN, C. JOHNSON AND E. TADMOR, *Essentially non-oscillatory and weighted essentially non-oscillatory schemes for hyperbolic conservation laws,* SIAM J. Sci. Stat. Comput., (11) (2006), pp. 325–432.

[52] C.-W. SHU AND S. OSHER, *Efficient implementation of essentially non-oscillatory shock-capturing schemes,* J. Computat. Phys., 77(2) (1988), pp. 439–471.

[53] C.-W. SHU AND S. OSHER, *Efficient implementation of essentially non-oscillatory shock-capturing schemes, II,* J. Computat. Phys., 83(1) (1989), pp. 32–78.

[54] J. STEGER AND R. F. WARMING, *Flux vector splitting of the inviscid gas dynamics equations with application to finite difference methods,* J. Computat. Phys., 40(05) (1981), pp. 263–293.

[55] V. A. TITAREV AND E. F. TORO, *Flux vector splitting of the inviscid gas dynamics equations with application to finite difference methods,* J. Computat. Phys., 201(1) (2004), pp. 238–260.

[56] E. F. TORO, M. SPRUCE AND W. SPEARES, *Restoration of the contact surface in the HLL-Riemann solver,* Shock Waves, 4(1) (1994), pp. 25–34.

[57] B. VAN LEER, *Flux-vector splitting for the Euler equations,* Eighth International Conference on Numerical Methods in Fluid Dynamics, Berlin, Heidelberg, Springer Berlin Heidelberg, (1982), pp. 507–512.

[58] Z. WANG, J. ZHU, Y. YANG, L. TIAN AND N. ZHAO, *A class of robust low dissipation nested multi-resolution WENO schemes for solving hyperbolic conservation laws,* Adv. Appl. Math. Mech., 13 (2021), pp. 1064–1095.

[59] B. WENDROFF, *A two-dimensional HLLE Riemann solver and associated Godunov-type difference scheme for gas dynamics,* Comput. Math. Appl., 38(11) (1999), pp. 175–185.

[60] G. ZHA AND E. BILGEN, *A two-dimensional HLLE riemann solver and associated Godunov-type difference scheme for gas dynamics,* Int. J. Numer. Methods Fluids, 17(07) (1993), pp. 115–144.

[61] B. ZHOU, F. QU, D. SUN, Z. WANG AND J. BAI, *A study of higher-order reconstruction methods for genuinely two-dimensional Riemann solver,* J. Computat. Phys., 443 (2021), 110469.